Journal of Groundwater Science and Engineering
ISSN 2305-7068
Indexed by ESCI CABI CSA
Scopus GeoRef AJ CNKI

Spatiotemporal dynamics of water table depth in Southwest China (1958–2015) under complex hydrogeological settings

Zheng Lu, De-hui Ning, Hui-bin Yang, Hai-rui Hao, Li-min Liao, Xi-xi Lan, Cheng-zhi Hao, Xu Zhou, Juan Bai, Jin-hui Wu, Sha-sha Meng

Citation:
Lu Z, Ning DH, Yang HB, Hao HR, Liao LM, Lan XX, Hao CZ, Zhou X, Bai J, Wu JH, Meng SS. 2026. Spatiotemporal dynamics of water table depth in Southwest China (1958–2015) under complex hydrogeological settings. Journal of Groundwater Science and Engineering, 14(4): 493-517.

View online: https://doi.org/10.26599/JGSE.2026.9280091

Articles you may be interested in

Attenuation of hydroclimatic influence on groundwater dynamics under anthropogenic stress: A decadal spatiotemporal analysis in Jaipur, India
Journal of Groundwater Science and Engineering. 2026, 14(3): 288-306 https://doi.org/10.26599/JGSE.2026.9280086

Groundwater recharge modeling with integration of land use/land cover and climate change projections in Surakarta City, Indonesia
Journal of Groundwater Science and Engineering. 2025, 13(4): 352-370 https://doi.org/10.26599/JGSE.2025.9280059

Karst distribution characteristics in a watershed under topographic differentiation and implication for groundwater resource: A case study in Southwest China using ERT and borehole data
Journal of Groundwater Science and Engineering. 2026, 14(3): 271-287 https://doi.org/10.26599/JGSE.2026.9280083

Identification of groundwater potential in hard rock aquifer systems using Remote Sensing, GIS and Magnetic Survey in Veppanthattai, Perambalur, Tamilnadu
Journal of Groundwater Science and Engineering. 2022, 10(4): 367-380 https://doi.org/10.19637/j.cnki.2305-7068.2022.04.005

Application of the DITAPH model coupling human activities and groundwater dynamics for nitrate vulnerability assessment: A case study in Quanzhou, China
Journal of Groundwater Science and Engineering. 2026, 14(1): 32-48 https://doi.org/10.26599/JGSE.2026.9280069

The effect of beach slope variation on saltwater intrusion dynamics in the unconfined coastal aquifer (experimental and numerical)
Journal of Groundwater Science and Engineering. 2026, 14(2): 165-187 https://doi.org/10.26599/JGSE.2026.9280077

Journal homepage: http://gwse.iheg.org.cn

Research Article

Spatiotemporal dynamics of water table depth in Southwest China (1958–2015) under complex hydrogeological settings

Zheng Lu[1], De-hui Ning[1], Hui-bin Yang[2], Hai-rui Hao[3], Li-min Liao[4], Xi-xi Lan[1], Cheng-zhi Hao[5], Xu Zhou[6], Juan Bai[7], Jin-hui Wu[8*], Sha-sha Meng[9*]

[1] *Faculty of Electric Power Engineering*, *Kunming University of Science and Technology*, *Kunming* 650500, *China*.
[2] *School Of Resources Engineering*, *Yunnan Tourism College*, *Kunming* 650221, *China*.
[3] *Department of Atmospheric Sciences*, *Yunnan University*, *Kunming* 650500, *China*.
[4] *Powerchina Kunming Engineering Corporation Limited*; *Kunming* 650051, *China*.
[5] *Hainan Provincial Ecological and Environmental Monitoring Centre*, *Haikou* 571126, *China*.
[6] *State Key Laboratory of Earth Surface Processes and Disaster Risk Reduction*, *Beijing Normal University*, *Beijing* 100875, *China*.
[7] *China Aero Geophysical Survey and Remote Sensing Center for Natural Resources*, *China Geological Survey*, *Beijing* 100083, *China*.
[8] *China Institute of Geo-Environment Monitoring*, *China Geological Survey*, *Beijing* 100081, *China*.
[9] *School of Geography*, *Faculty of Geographical Science*, *Beijing Normal University*, *Beijing* 100875, *China*.

Abstract: Groundwater provides an essential buffer against hydroclimatic variability in monsoon-influenced regions, yet its long-term dynamics and interactions with human activities remain poorly constrained in complex hydrogeological settings such as Southwest China (SWC). This study integrates outputs from the high-resolution PCRaster Global Water Balance model (PCR-GLOBWB) with spatial statistics to examine temporal evolution, spatial heterogeneity, and anthropogenic influences on Water Table Depth (WTD) from 1958 to 2015. Results reveal a persistent long-term rise in groundwater levels (i.e., a decline in WTD) at a Sen's slope of –0.0285 m/y, with episodic drawdowns during drought years and only partial recovery in subsequent wet periods. Seasonal oscillations remain pronounced, with the shallowest water tables occurring in late summer and the deepest in spring, although long-term depletion suggests that natural recharge is insufficient to balance cumulative extraction. Shallow aquifers (<1 m) are closely coupled with precipitation–evapotranspiration variability, while deeper systems (>5 m) are increasingly buffered and display inverse relationships, reflecting delayed recharge processes. Spatial patterns demonstrate strong heterogeneity across climate zones, geomorphic units, land cover types, and aquifer types: Shallow groundwater is concentrated in semi-arid climates, lowland plains, and urban areas, whereas mountainous regions, undeveloped land, and discontinuous carbonate aquifers sustain deeper and more variable WTDs. Anthropogenic stress further modulates these distributions, with bivariate LISA analysis identifying High–High clusters (intensive human modification and deep water tables) in the Chengdu Plain and central Yunnan, and Low–Low clusters in sparsely populated western highlands. A groundwater protection zoning framework derived from these results highlights shallow aquifers under intensive stress as priority areas for monitoring and regulation. These findings demonstrate the coupled influence of climate and human activity on groundwater variability and provide a practical basis for regionally targeted management strategies to enhance groundwater sustainability in SWC.

Keywords: Groundwater; Spatiotemporal dynamics; Geomorphology; Land cover; Karst aquifer systems; Anthropogenic stress

Received: 16 Nov 2025/ Accepted: 07 Apr 2026/ Published: 10 Oct 2026

[*]Corresponding author: Jin-hui Wu, Sha-sha Meng, *E-mail address*: jwu@mail.cgs.gov.cn, mengshasha@mail.bnu.edu.cn

DOI: 10.26599/JGSE.2026.9280091

Lu Z, Ning DH, Yang HB, et al. 2026. Spatiotemporal dynamics of water table depth in Southwest China (1958–2015) under complex hydrogeological settings. Journal of Groundwater Science and Engineering, 14(4): 493-517.

2305-7068/© 2026 Journal of Groundwater Science and Engineering Editorial Office This is an open access article under the CC BY-NC-ND license (http://creativecommons.org/licenses/by-nc-nd/4.0)

Introduction

Groundwater represents a critical freshwater resource globally, sustaining ecosystems and human societies through its role in water supply, agricultural irrigation, and baseflow maintenance, particularly in monsoon-dominated regions of Asia (Brooks et al., 2025; Gleeson et al., 2020; Kuang et

al., 2024; Scanlon et al., 2023). Despite its importance, large-scale assessments of groundwater dynamics remain limited due to the inherent complexity of subsurface processes and limited observational data (Fang et al., 2015; Jasechko et al., 2024). Water Table Depth (WTD) is a key indicator of groundwater conditions, reflecting the balance between recharge, discharge, and anthropogenic influences (Cuthbert et al., 2019; Fan et al., 2013; Maxwell and Condon, 2016). However, current understanding of WTD dynamics remains inadequate, particularly regarding its response to human modification and climate variability across heterogeneous landscapes (Huggins et al., 2025; Taylor et al., 2013; Zhong et al., 2025).

Previous research has highlighted several gaps in groundwater studies. While numerous studies have documented groundwater depletion globally, the spatial patterns and mechanisms of human–groundwater interactions remain poorly characterized at regional scales (Maina et al., 2024; Shen et al., 2025; Wada et al., 2010). Existing assessments often rely on sparse monitoring networks (Berghuijs et al., 2022; Chávez García Silva et al., 2024; Moeck et al., 2020; Longhuan Wang et al., 2024) or simplified models that inadequately represent complex hydrogeological settings (Akhter et al., 2025; Reinecke et al., 2024). Although spatial heterogeneity has been recognized, systematic analyses across multiple environmental factors, such as climate, geomorphology, land cover, and aquifer type, are still limited (Fan et al., 2019; Gnann et al., 2025; Lu et al., 2024). Moreover, shallow aquifers have been more extensively studied than deeper systems, leaving questions about how groundwater at different depths responds to Precipitation–EvapoTranspiration (P–ET) variability (Akhter et al., 2025; Zhou et al., 2023). Furthermore, the integration of anthropogenic stress indicators with WTD variability has received limited attention, particularly in developing regions where groundwater exploitation is intensifying (Asoka et al., 2017; Gurdak, 2017; MacAllister et al., 2022; Tanguy et al., 2023). The absence of high-resolution, spatially explicit analyses of human–groundwater interactions represents a critical knowledge gap in sustainable water resources management (Curran et al., 2023; Long et al., 2025; Meles et al., 2024).

Recent advancements in hydrological modeling, remote sensing, and data assimilation have created new opportunities to address these limitations. Improved global-scale groundwater models (van Jaarsveld et al., 2025; Verkaik et al., 2024), enhanced satellite-based monitoring techniques (Adams et al., 2022; Rodell and Reager, 2023), and sophisticated spatial analysis methods (Hu et al., 2022; Liu et al., 2021) now enable more comprehensive characterization of groundwater systems. Concurrently, the development of global anthropogenic stress datasets (Kennedy et al., 2019) provides unprecedented capacity to quantify human impacts on hydrological systems. These technological and methodological advances facilitate the integration of physical processes and human dimensions in groundwater assessments.

Despite this progress, significant challenges remain in regions characterized by complex hydrogeological settings. Southwest China (SWC) presents a particularly compelling case study, characterized by extreme topographical variability, extensive karst formations, and rapidly intensifying human pressures (Hao et al., 2025; Liu et al., 2021; Shu et al., 2023; Yin et al., 2021). The intricate river networks, heterogeneous lithology, and monsoon-dominated climate create complex groundwater dynamics that are poorly represented in existing global assessments (Huang et al., 2019; Li et al., 2017; Wang et al., 2025). Furthermore, the impacts of anthropogenic stress on WTD variability in this hydrogeologically complex region remain essentially unexplored, despite its critical importance for water security in one of China's most rapidly developing regions (Wu et al., 2023; Xing et al., 2024).

This study addresses these challenges by conducting a comprehensive spatiotemporal assessment of groundwater dynamics across SWC from 1958 to 2015 using outputs from PCRaster Global Water Balance model (PCR-GLOBWB) (van Beek et al., 2011; Verkaik et al., 2024) integrated with statistical and spatial analyses. Specifically, the objectives are: (1) to quantify long-term and seasonal variations in WTD and evaluate depth-dependent relationships with P–ET; (2) to characterize spatial heterogeneity of WTD across climatic zones, geomorphic units, land cover types, and karst aquifer systems; and (3) to analyze how anthropogenic stress interacts with groundwater variability using spatial correlation and bivariate LISA approaches. Through these objectives, we seek to provide new insights into human-groundwater interactions in complex hydrogeological settings and contribute to improved groundwater management strategies.

1 Study area

SWC, including Yunnan, Guizhou, Sichuan, Chongqing, and Guangxi, is situated in a complex

physiographic transition zone between the Tibetan Plateau and the lowlands of Southeast China (Fig. 1a). The region is characterized by pronounced topographic variability, with elevations ranging from <500 m in the southeastern basins to >7,000 m along the northwestern plateau margins. Several principal rivers, including the upper Yangtze and Pearl River tributaries, drain the region and form critical water sources for downstream ecosystems and human activities. Climatically, SWC spans humid to semi-arid zones, with mean annual precipitation ranging from about 500 mm to more than 2,600 mm, showing strong spatial gradients associated with the East Asian monsoon (Fig. 1c–1d) (Wang et al., 2025; Wu et al., 2024; Zomer et al., 2022). Geomorphologically, the landscape is composed of plains, hills, plateaus, and extensive mountain ranges (Fig. 1e). The region also hosts the world's largest continuous karst terrain, mainly distributed across Guizhou, Guangxi, and parts of Yunnan, which exerts strong controls on hydrological processes due to its unique hydrogeological

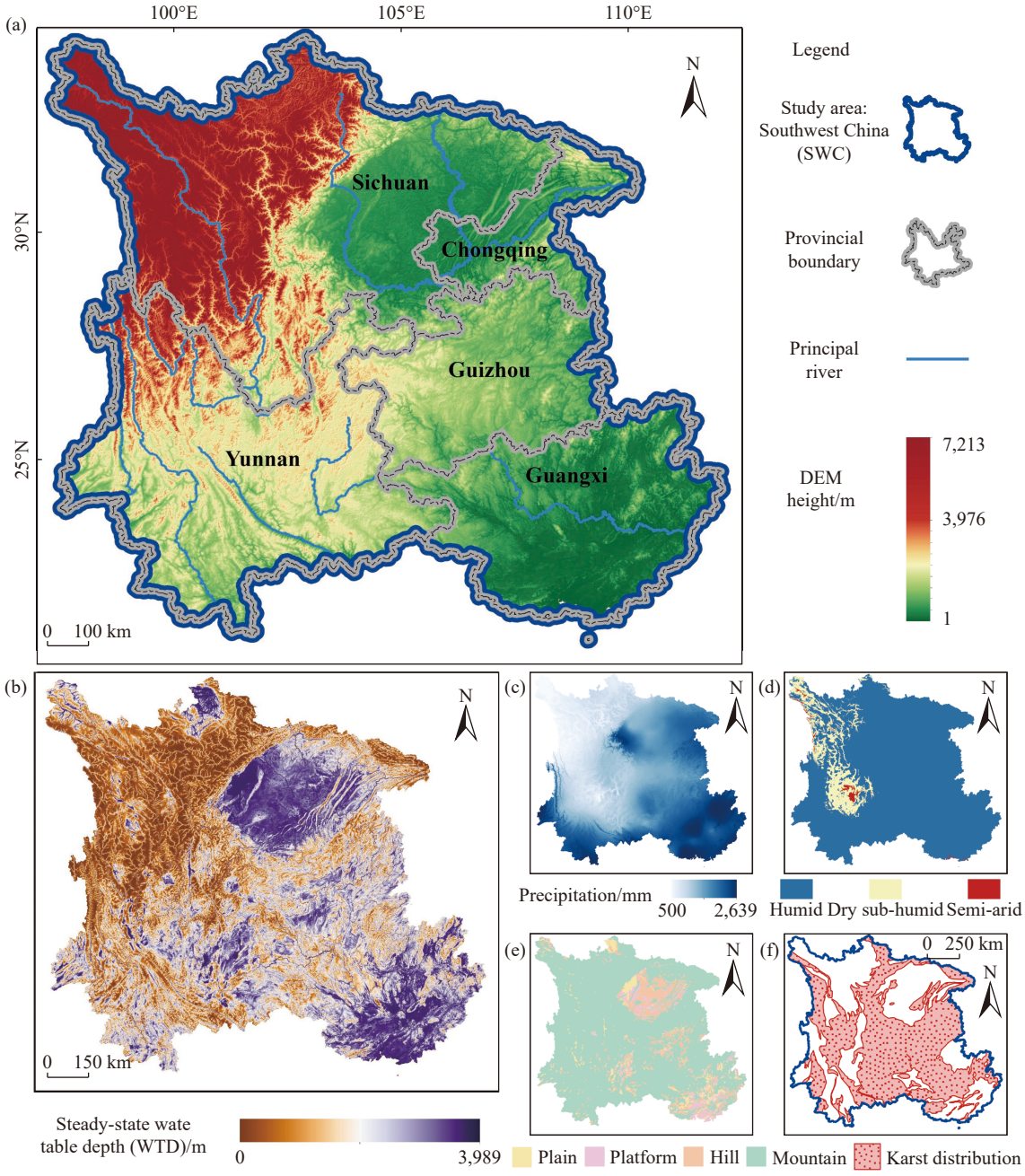


Fig. 1 Overview and maps of the study area, Southwest China (SWC)

Notes: (a) regional location with DEM, provincial boundaries, and river networks; (b) steady-state water table depth (WTD) based on the GLOBGM v1.0 dataset (Verkaik et al., 2024); (c) multi-year average precipitation (Peng et al., 2019); (d) climate zoning based on the aridity index (Zomer et al., 2022); (e) geomorphic units (Geomorphological Map of China); (f) karst aquifer extent (World Karst Aquifer Map, WOKAM)

properties (Fig. 1f) (Ford and Williams, 2007; Hu et al., 2024).

The distribution of steady-state WTD reflects the combined influence of these climatic, geomorphic, and hydrogeological factors (Fig. 1b). Shallow WTD occurs predominantly in humid lowland plains and river valleys, where abundant precipitation and favorable hydrogeological conditions promote recharge and sustain groundwater levels. In contrast, deeper WTD is evident in high-elevation or semi-arid zones, where steep terrain, limited infiltration, the presence of low-permeability sediments and rocks at depth, as well as higher evaporative demand, reduce recharge potential. Karst regions exhibit complex WTD variability due to heterogeneous subsurface structures and rapid infiltration pathways. Collectively, the spatial heterogeneity in precipitation, evapotranspiration demand, topography, and lithology jointly governs the regional groundwater distribution pattern (Li et al., 2023; Shi et al., 2024).

2 Methodology

This section begins by describing the datasets and preprocessing procedures, followed by the methodological approaches. An overview of the workflow is provided in Fig. 2.

2.1 Datasets and preprocessing

The WTD data utilized in this study were derived from the PCRaster Global Water Balance model (PCR-GLOBWB) (van Beek et al., 2011), referred to as GLOBGM v1.0 (Verkaik et al., 2024) in the following. The model is a parallel implementation of a 30" (arc-second) PCR-GLOBWB-MODFLOW global-scale groundwater model (de Graaf et al., 2017). This model represents a significant advancement over its 5' (arcminute) predecessor, offering substantially enhanced spatial resolution of approximately 1 km at the equator. The GLOBGM model has two vertical layers: an upper confining layer (where present) and a lower aquifer layer, employing unstructured grids to eliminate redundant sea and land cells while maintaining all necessary boundary conditions (Verkaik et al., 2024). For this study, we extracted WTD data for SWC from the Afro-Eurasia continental-scale model segment, including 1,784,284 valid grids.

All spatial datasets used in this analysis, including anthropogenic stress indicators and climatic variables, were resampled to match this 30" spatial resolution to ensure dimensional consistency across all analyses. Data preprocessing involved masking out invalid values and negative values, which were converted to no-data to exclude them

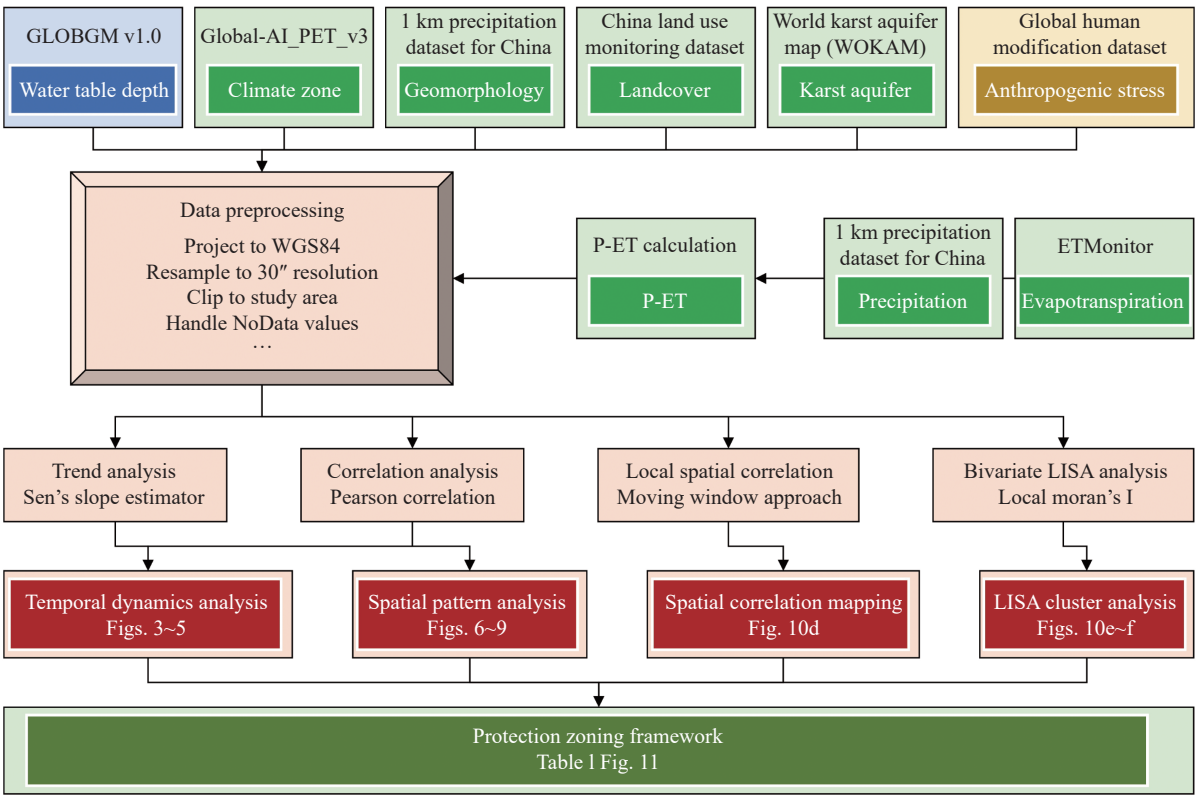


Fig. 2 Schematic diagram of the overall methodology and data processing workflow

from subsequent analysis. Quality control procedures included spatial consistency checks between datasets, with necessary reprocessing using bilinear interpolation to maintain alignment with the 30" reference framework. Prior to the analysis, the GLOBGM WTD data were validated against in-situ groundwater well observations from 17 monitoring wells with precise coordinates across SWC. The validation results showed a correlation coefficient (R) of 0.807, a Root Mean Square Error (RMSE) of 19.39 m, and a bias of 12.06 m, indicating that the GLOBGM product possesses reasonable accuracy and is capable of capturing the spatiotemporal characteristics of water table dynamics, particularly in shallow aquifers.

Precipitation (P) data were obtained from a high-resolution (1 km) monthly dataset for China (1901–2024), processed through delta spatial downscaling of the CRU and WorldClim datasets (Peng et al., 2019). The NetCDF format data were extracted, clipped to the study area, and resampled to 30" resolution. Evapotranspiration (ET) data were derived from the global ETMonitor dataset (1 km resolution), incorporating multi-source satellite inputs and ERA5 reanalysis data (Zheng et al., 2022). The ET data were reprojected to WGS84, clipped to the study region, and aggregated to monthly values. The precipitation minus evapotranspiration (P–ET) balance was calculated at 30" resolution to represent atmospheric water available for potential groundwater recharge, producing a monthly time series from 2003 to 2015 for analyzing hydrological relationships across different water table regimes.

The climate zoning data were derived from the Global Aridity Index and Potential Evapotranspiration Database (Global-AI_PET_v3), which provides high-resolution (30") global hydro-climatic data based on the FAO Penman-Monteith Reference Evapotranspiration equation, with aridity index values classified into hyper-arid (<0.03), arid (0.03–0.20), semi-arid (0.20–0.50), dry sub-humid (0.50–0.65), and humid (>0.65) zones (Zomer et al., 2022). The geomorphology and land cover data are available at the Resource and Environmental Science Data Platform (https://www.resdc.cn/). Specifically, the geomorphology dataset was obtained from the 1:1 million scale Geomorphological Map of China, which comprehensively reflects macro-scale geomorphological patterns and spatial differentiation through a hierarchical classification system encompassing basic geomorphological types and morphological structures based on genesis, elevation, and relief amplitude. Land cover data (DOI: 10.12078/2018070201) were sourced from the China Multi-Period Land Use Remote Sensing Monitoring Dataset, which employs a two-level classification system with six primary categories (cropland, forest, grassland, water, urban, and unused land) and twenty-five secondary categories based on Landsat imagery and manual visual interpretation, providing national-scale land cover information for multiple periods since the 1980s. All datasets were clipped to the study area and resampled to 30" resolution to ensure spatial consistency with other data layers.

The karst aquifer extent data utilized in this study were derived from the World Karst Aquifer Map (WOKAM), which classifies global carbonate and evaporite formations into continuous (>65% karstifiable rock) and discontinuous (15%–65% karstifiable rock) categories based on lithological predominance (Chen et al., 2017). This dataset was developed through systematic processing of the Global Lithological Map (GLiM) (Hartmann and Moosdorf, 2012), enhanced by regional geological validation and expert review, and subsequently rasterized at a global-scale resolution to support hydrogeological analysis and spatial modeling of karst groundwater systems.

The anthropogenic stress data utilized in this study were derived from the Global Human Modification Dataset developed by Kennedy et al., (2019), which provides a cumulative measure of human modification across terrestrial lands. This dataset integrates thirteen anthropogenic stressors using a fuzzy algebraic sum aggregation method to compute a continuous modification gradient ranging from 0 (no modification) to 1 (high modification). The original data at 1 km resolution were acquired in geographic coordinates (WGS84) and preprocessed to ensure spatial consistency with other datasets. Specifically, the anthropogenic stress data were clipped to the SWC study region using a geographic mask and resampled to 30" resolution to align with the spatial reference and resolution of the WTD data. All raster processing, including projection to the required coordinate system and resampling, was performed using ArcGIS (ESRI) with the Spatial Analyst extension to maintain data integrity and spatial accuracy throughout the analysis.

2.2 Methods

All statistical analyses incorporated appropriate significance testing methods. For correlation analyses, we used t-tests for Pearson correlations and permutation tests for Spearman correlations. For

spatial analyses, we employed conditional permutation tests that account for spatial autocorrelation in the data. Sensitivity analyses were conducted to evaluate the robustness of results to methodological choices, including window size for local correlations and neighborhood definition for spatial weights. Results were consistent across these variations, indicating methodological robustness. All spatial statistical analyses were implemented in MATLAB or R with custom algorithms developed for this study, leveraging the Mapping Toolbox for geospatial data processing and visualization.

2.2.1 Trend analysis using Sen's slope estimator

To quantify long-term trends in WTD, we employed the non-parametric Sen's slope estimator, which is robust to outliers and non-normal data distributions (Ahmad et al., 2025; Lu et al., 2017). The Sen's slope (β) represents the median of all possible slopes between paired data points in a time series and is calculated as (Sen, 1968):

$$\beta = \left(\frac{x_b - x_a}{b - a}\right), \text{for all } b < a \tag{1}$$

Where: x_a and x_b represent values at time points a and b, respectively. This method is particularly suitable for hydrological time series as it does not assume a normal distribution of residuals and is less sensitive to extreme values than linear regression (Akritas et al., 1995; Mehboob and Kim, 2024).

2.2.2 Correlation analysis

We conducted comprehensive correlation analyses to examine relationships between WTD and various environmental or anthropogenic factors, including P–ET and anthropogenic stress in this study. Pearson correlation coefficient (R) was used to assess linear relationships between variables (Lu et al., 2023):

$$R = \frac{\sum_{c=1}^{m}(x_c - \bar{x})(y_c - \bar{y})}{\sqrt{\sum_{c=1}^{m}(x_c - \bar{x})^2 (y_c - \bar{y})^2}} \tag{2}$$

Where: x_c and y_c represent paired observations, and $\bar{x}$ and $\bar{y}$ are their respective means.

2.2.3 Local spatial correlation analysis using moving window approach

To explore spatial non-stationarity in the relationship between WTD and anthropogenic stress, we implemented a moving window approach to compute local correlation coefficients across the study area. This method calculates correlation coefficients within a defined spatial neighborhood around each pixel, capturing local variations in the WTD-anthropogenic stress relationship (Jalili et al., 2016; Lu et al., 2025b).

A 5×5 pixel window was employed, representing an optimal balance between spatial resolution and statistical reliability. For each grid location (i, j), we extracted all valid WTD and anthropogenic stress values within the window and computed the Pearson correlation coefficient. Only windows containing at least three valid pixel pairs were included in the analysis to ensure statistical robustness. The local correlation coefficient r_{ij} at grid location (i, j) was calculated as (Blaschke et al., 2024; Ord and Getis, 1995):

$$r_{ij} = \frac{\sum_{i,j=1}^{n_{ij}} \left(WTD_{ij} - \overline{WTD}_{ij}\right)\left(AS_{ij} - \overline{AS}_{ij}\right)}{\sqrt{\sum_{i,j=1}^{n_{ij}} \left(WTD_{ij} - \overline{WTD}_{ij}\right)^2 \left(AS_{ij} - \overline{AS}_{ij}\right)^2}} \tag{3}$$

Where: WTD_{ij} and AS_{ij} represent the WTD and anthropogenic stress values at grid location (i, j), respectively, and $\overline{WTD}$ and $\overline{AS}$ represent their mean values. n_{ij} represents the number of valid pixels within the window centered at grid location (i, j).

2.2.4 Bivariate Local Indicators of Spatial Association (LISA) analysis

To evaluate spatial dependence between WTD and anthropogenic stress, a bivariate Local Indicators of Spatial Association (LISA) framework was applied using Moran's I statistic (Anselin, 1995). Moran's I is a measure of spatial autocorrelation, where a positive value indicates clustering of similar values, and a negative value indicates clustering of dissimilar values. This method identifies localized clusters where high or low values of WTD are systematically associated with high or low values of anthropogenic stress, thereby providing insight into spatial heterogeneity in human–groundwater interactions (Mao et al., 2024).

The bivariate LISA for a given location i was defined as (Anselin, 1995):

$$I_i^b = Z_{WTD_i} \sum_{j=1}^{n} \omega_{ij} Z_{AS_j} \tag{4}$$

Where: Z_{WTD_i} represents the standardized WTD value at location i, calculated as:

$$Z_{WTD_i} = \frac{(WTD_i - \mu_{WTD})}{\sigma_{WTD}} \tag{5}$$

Where: μ_{WTD} and σ_{WTD} denote the mean and standard deviation of WTD, respectively. Similarly, Z_{AS_j} represents the standardized anthropogenic

stress value at neighboring location j. The spatial weight between locations i and j is denoted by ω_{ij}, and n indicates the number of neighboring locations included in the analysis.

Spatial weights were defined using a queen's case contiguity matrix with a distance threshold to ensure inclusion of diagonal neighbors (Anselin et al., 2007):

$$Distance\ threshold = \sqrt{2} \times grid\ size + 0.001 \quad (6)$$

Where: grid size is 30" in this study. The weights matrix was row-standardized:

$$\sum_{j=1}^{n} \omega_{ij} = 1 \quad (7)$$

Statistical significance was assessed through a permutation approach with 999 randomizations to generate reference distributions under the null hypothesis of spatial randomness (Liu et al., 2024). The p-value for each location i was calculated as:

$$p_i = \frac{\sum_{k=1}^{999} \left|\left| \left(I_{i,k}^{perm} \geq I_i\right) \right|\right| + 1}{1000} \quad (8)$$

Where: The operator ‖·‖ represents the indicator function that takes the value 1 when the condition is satisfied and 0 otherwise, $I_{i,k}^{perm}$ denotes the LISA statistic for the k-th permutation at location i, and I_i represents the observed LISA statistic. The addition of 1 in both numerator and denominator ensures that p-values cannot equal zero.

Local spatial associations were classified according to the sign and significance of the statistic, in combination with the relative magnitudes of standardized variables. Statistically significant ($p < 0.05$) positive associations were designated as High–High clusters when large WTD values co-occurred with elevated anthropogenic stress ($z > 0$), or as Low–Low clusters when shallow WTD coincided with reduced stress ($z < 0$). Significant negative associations were categorized as High–Low clusters (deep WTD with low stress) or Low–High clusters (shallow WTD with high stress). Non-significant results ($p \geq 0.05$) were interpreted as lacking detectable local spatial association.

The analysis was conducted in R (v4.4.2) using the *terra*, *sf* and *spdep* packages. The analytical procedure consisted of sequential steps: Variable standardization, neighborhood definition, LISA computation, significance testing through permutation, classification of spatial association types, and cartographic visualization at 30" resolution. By extending traditional univariate Moran's I to a bivariate context, this approach provides a robust framework to capture local-scale dependencies between groundwater levels and human pressures, while explicitly accounting for spatial autocorrelation (Anselin et al., 2007; Mao et al., 2024).

3 Results

This section presents a comprehensive analysis of both temporal dynamics and spatial patterns of WTD across SWC from 1958 to 2015. We first analyzed the long-term trends and seasonal variations in WTD. The relationship between shallow groundwater systems and P–ET is then investigated. Based on spatial analyses, we further explored how WTD distributions vary across climate zones, geomorphological units, land cover types, and karst aquifer systems. Finally, we analyzed the impacts of anthropogenic pressures on groundwater variability.

3.1 Temporal dynamics of water table depth

3.1.1 Long-term and seasonal variations in water table depth

Fig. 3 presents a comprehensive analysis of WTD variations in SWC from 1958 to 2015. The annual mean series (Fig. 3a) reveals considerable interannual variability, superimposed on a significant long-term trend. The calculated Sen's slope of –0.0285 m/y indicates a sustained decrease in WTD over the study period, corresponding to a long-term rise in groundwater level. This trend of increasing water levels is punctuated by episodic drawdowns, most notably during the early 2000s, coinciding with widespread drought conditions. Despite these dry-period declines, the overarching six-decade progression indicates a net shallowing of the water table. These findings suggest a complex interplay where natural hydroclimatic variability drives strong interannual fluctuations, but the long-term trend reflects other balancing factors in the regional groundwater system.

Seasonal dynamics are highlighted in the monthly WTD series (Fig. 3b), which shows a consistent oscillatory pattern driven by monsoonal precipitation regimes. Water tables typically reach their shallowest levels between July and September, coinciding with peak monsoon rainfall and enhanced recharge, and deepen markedly during the dry season months of February to April. This pattern has remained robust throughout the study period, underscoring the strong climatic imprint on

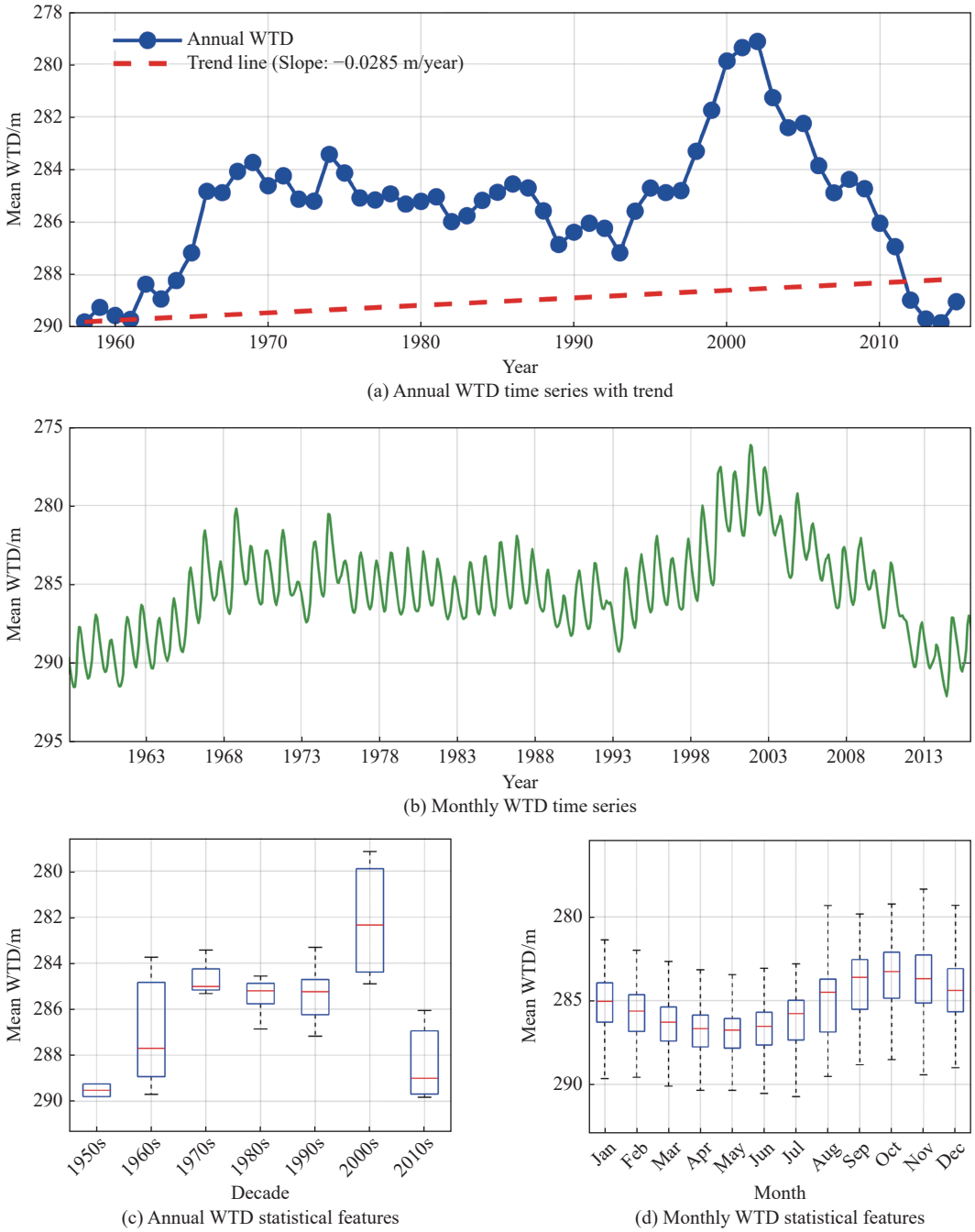


Fig. 3 Temporal variations and statistical characteristics of Water Table Depth (WTD) in Southwest China (SWC) (1958–2015): (a) annual mean WTD time series showing a long-term decreasing trend (Sen's slope = –0.0285 m/y, indicating rising groundwater levels), (b) monthly WTD time series, (c) inter-decadal statistical characteristics of annual WTD, and (d) monthly statistical characteristics of WTD

groundwater systems. However, the gradual lowering of baseline levels across decades points to a cumulative imbalance between recharge and extraction, whereby natural recharge is insufficient to offset long-term withdrawals and landscape changes.

The statistical boxplots (Fig. 3c, 3d) further distill these temporal characteristics into decadal and monthly perspectives. The decadal summary (Fig. 3c) reveals a progressive shift toward shallower WTD (higher groundwater levels), with the 2000s and 2010s exhibiting significantly lower medians and expanded ranges relative to earlier decades, indicating increasing variability in groundwater conditions in recent decades. Monthly boxplots (Fig. 3d) capture systematic intra-annual variability, with the shallowest distributions observed during the wet season and the deepest

during the late dry season. Together, these results illustrate a dual signal: Strong climatic seasonality superimposed on a long-term declining WTD trajectory. This combination highlights both the hydroclimatic sensitivity of the aquifer system and its increasing vulnerability under intensifying anthropogenic stress.

Here we further analyze the seasonal and intra-annual variability of WTD across SWC (Fig. 4). The monthly cycle (Fig. 4a) reveals a clear hydroclimatic signal, with the shallowest groundwater levels occurring between September and October, following peak monsoonal recharge. Conversely, the largest WTD values are observed from March to May, prior to the onset of the rainy season, when soil moisture deficits and sustained evapotranspiration draw down aquifer storage. This seasonal oscillation, averaging 6–8 m between maximum and minimum bounds, underscores the strong coupling between precipitation seasonality and groundwater dynamics, consistent with other monsoon-influenced regions of Asia (Wang et al., 2025; Wu et al., 2024).

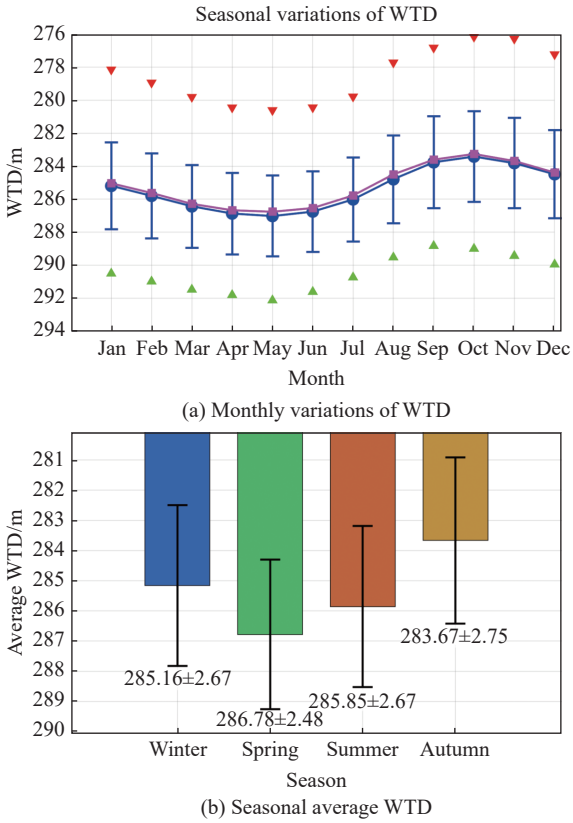


Fig. 4 Seasonal patterns of Water Table Depth (WTD) variations in Southwest China (1958–2015)

Notes: (a) monthly variations showing mean values with standard deviation error bars, extreme values (minimum and maximum), and median WTD across all years; (b) inter-seasonal comparison of average WTD with standard deviation error bars, highlighting differences between winter (Dec-Feb), spring (Mar-May), summer (Jun-Aug), and autumn (Sep-Nov)

The seasonal averages (Fig. 4b) further highlight the phase-dependent fluctuations. Autumn registers the shallowest mean water table (283.67 ± 2.75 m), reflecting post-monsoon aquifer recharge, whereas spring exhibits the deepest mean (286.78 ± 2.48 m), reflecting the cumulative impact of prolonged dry-season depletion. Winter and summer represent transitional states, with averages of 285.16 ± 2.67 m and 285.85 ± 2.67 m, respectively. The relatively higher uncertainty during autumn compared to other seasons indicates stronger interannual variability in recharge efficiency, likely influenced by spatial heterogeneity in rainfall distribution, irrigation return flows, and land-use change (Li et al., 2017; Liu et al., 2021; Lin Wang et al., 2024).

Taken together, these results demonstrate the dual control of climate and human water use on groundwater seasonality in SWC. While the monsoonal cycle defines the broad recharge–depletion rhythm, anthropogenic pressures, including intensified dry-season pumping for agriculture and urban supply, exacerbate spring drawdowns and attenuate natural recovery during autumn. The persistence of this cycle over six decades indicates resilience of the recharge–discharge system; however, the observed long-term deepening trend (Fig. 3) suggests that seasonal recovery has become insufficient to counterbalance cumulative extraction (Jiang et al., 2008; Shu et al., 2023; Yin et al., 2021). These findings emphasize the importance of considering both intra-annual dynamics and long-term trajectories when evaluating groundwater sustainability under ongoing climate variability and human modification.

3.1.2 Relationship between shallow water table depth and precipitation–evapotranspiration

Fig. 5 presents the temporal relationship between depth-specific Water Table Depth (WTD) and co-located precipitation minus evapotranspiration (P–ET). For four WTD thresholds (0–0.1 m, 0–1 m, 0–5 m, 0–10 m), we calculated annual WTD and P–ET anomalies by averaging over all pixels within the SWC region that met the respective depth criterion. This yields paired, depth-stratified annual time series (2003–2015) where WTD and P–ET values are spatially consistent, allowing for a direct analysis of their coupling. The analysis focuses on shallow groundwater because the exchange between atmospheric water (P–ET) and groundwater primarily occurs in the shallow subsurface. Deep groundwater is less directly

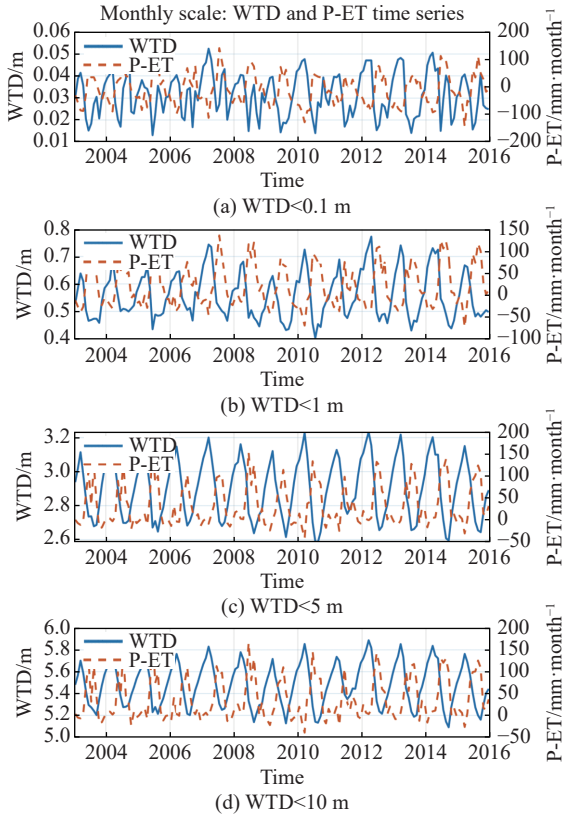


Fig. 5 Time series and correlation between depth-specific, co-located Water Table Depth (WTD) and precipitation–evapotranspiration (P–ET) anomalies for different WTD thresholds: (a) WTD < 0.1 m; (b) WTD < 1 m; (c) WTD < 5 m; (d) WTD < 10 m

influenced by short-term atmospheric fluxes due to damping and lag effects. Therefore, to understand the coupling between climate variability and groundwater responses, we limit the analysis to shallow WTD (≤10 m). This analysis further assesses the extent to which atmospheric water balance regulates groundwater fluctuations under varying aquifer thicknesses. Pearson correlation coefficient (R) was used as a statistical indicators of covariation, highlighting how hydrologic connectivity evolves as a function of WTD.

Fig. 5(a) shows that at extremely shallow groundwater depths (WTD < 0.1 m), the correlation between WTD and P–ET is strongly positive (R = 0.53). This is partly attributable to the direct and rapid exchange between soil moisture and the water table, where P–ET deficits (P–ET < 0) frequently occur. A negative P–ET value represents conditions in which evapotranspiration exceeds precipitation inputs, implying that atmospheric water demand surpasses supply (Rodell and Reager, 2023; Zhou et al., 2023). Under such conditions, shallow groundwater acts as a supplementary source to sustain evapotranspiration, reinforcing the coupling between WTD and P–ET. This mechanism explains the relatively high correlation at WTD < 0.1 m, as groundwater dynamics directly mirror short-term atmospheric forcing.

With increasing depth (WTD < 1 m), the strength of correlation decreases (R = 0.22, Fig. 5b), reflecting a buffering effect of the vadose zone that delays the transmission of precipitation and evapotranspiration signals to the water table (Habib, 2020; Lu and Yang, 2024). At intermediate depths (WTD < 5 m, Fig. 5c), the correlation becomes negative (R = –0.28), indicating that groundwater fluctuations are no longer synchronous with P–ET variations. This shift suggests that recharge processes are governed more by lateral subsurface flow and delayed infiltration rather than direct atmospheric drivers, consistent with findings in deeper semi-confined aquifers (Akhter et al., 2025; Chen et al., 2019; Stewart et al., 2025; Xu et al., 2023; Yang et al., 2018).

Interestingly, for deeper systems (WTD < 10 m in Fig. 5d), the correlation remains negative (R = –0.32), but the magnitude of P–ET anomalies is not markedly different from those observed at 5 m. This similarity reflects the fact that at greater depths, groundwater is increasingly disconnected from short-term atmospheric variability, and recharge processes are dominated by longer-term climatic accumulation or subsurface redistribution (Akhter et al., 2025; de Graaf et al., 2017; de Graaf and Stahl, 2022). In such settings, the role of P–ET as a direct control diminishes, and storage changes instead reflect integrated catchment-scale water balance processes.

Overall, these results demonstrate a depth-dependent relationship between atmospheric forcing and groundwater response, where shallow systems (< 1 m) are tightly coupled to P–ET variability, while deeper aquifers (> 5 m) exhibit a decoupled or inverse response due to buffering and delayed recharge dynamics.

3.2 Spatial patterns of water table depth

Building upon the temporal analysis, we now investigate the spatial distribution of WTD across Southwest China and its relationship with key environmental drivers. To systematically unravel the complex spatial controls, we analyze WTD variability across four critical environmental gradients: (i) climate zones (hydroclimatic control), (ii) geomorphological units (topographic and geological control), (iii) land cover types (surface process

and anthropogenic control), and (iv) karst aquifer types (hydrogeological control). This multi-faceted spatial framework allows for a comprehensive assessment of how regional hydroclimate, landscape structure, surface characteristics, and subsurface geology collectively shape the spatial heterogeneity of groundwater systems in this topographically and geologically diverse region.

3.2.1 Spatial distributions of water table depth over climate zones

Fig. 6 shows the spatial distribution of climate zones across SWC and the corresponding variability of WTD under different hydroclimatic regimes. The spatial patterns (Fig. 6a) demonstrate a predominance of humid zones, concentrated in the southeastern and central lowlands, while dry sub-humid and semi-arid regions are primarily localized in the western and transitional upland areas. The statistical comparison of WTD across climate types (Fig. 6b) reveals systematic differences that align with hydrological expectations. Semi-arid regions exhibit the smallest mean WTD (203.9 m). By contrast, dry sub-humid zones register the largest mean WTD (336.6 m), reflecting a combination of higher terrain, reduced infiltration efficiency, and limited aquifer replenishment. Humid areas fall in between (281.7 m), but the broader interquartile range in these zones suggests strong heterogeneity in recharge processes due to land use, soil permeability, and topographic gradients. These patterns corroborate earlier findings that climate-induced variability in infiltration and recharge rates can produce marked contrasts in groundwater depth across relatively small spatial scales (Condon et al., 2020; Taylor et al., 2013). While humid regions maintain comparatively moderate WTDs, the vulnerability of semi-arid and dry sub-humid zones to both natural variability and human modification is pronounced (Zhang et al., 2023), as even minor reductions in recharge or increases in pumping pressure can rapidly propagate into substantial groundwater stress (Huggins et al., 2025).

3.2.2 Spatial distributions of water table depth over geomorphology

Fig. 7 shows the spatial configuration of geomorphic units across SWC and their corresponding effects on WTD. The spatial distribution map (Fig. 7a) identifies four dominant geomorphological settings (plains, platforms, hills, and mountains), each characterized by distinct hydrogeological and recharge conditions. The statistical summary (Fig. 7b) demonstrates marked contrasts in WTD across these units, with shallow groundwater prevailing in plains (mean depth: 21.4 m) and platforms (26.6 m), intermediate depths in hilly regions (48.7 m), and substantially deeper groundwater levels in mountainous terrains (341.8 m).

These differences reflect the combined influence of geomorphology on recharge, storage, and discharge processes. Plains and platforms typically host unconsolidated alluvial deposits with relatively high porosity and transmissivity, enabling shallow water tables sustained by river–aquifer interactions and irrigation return flows (Feng and Gleason, 2024; Lu and Yang, 2024). In contrast, hilly landscapes exhibit steeper topography and thinner soils, which promote rapid runoff and limit infiltration, resulting in moderately deeper WTD (Fan et al., 2019; Gnann et al., 2025). Mountainous areas show the deepest water tables, shaped by fractured bedrock aquifers, steep

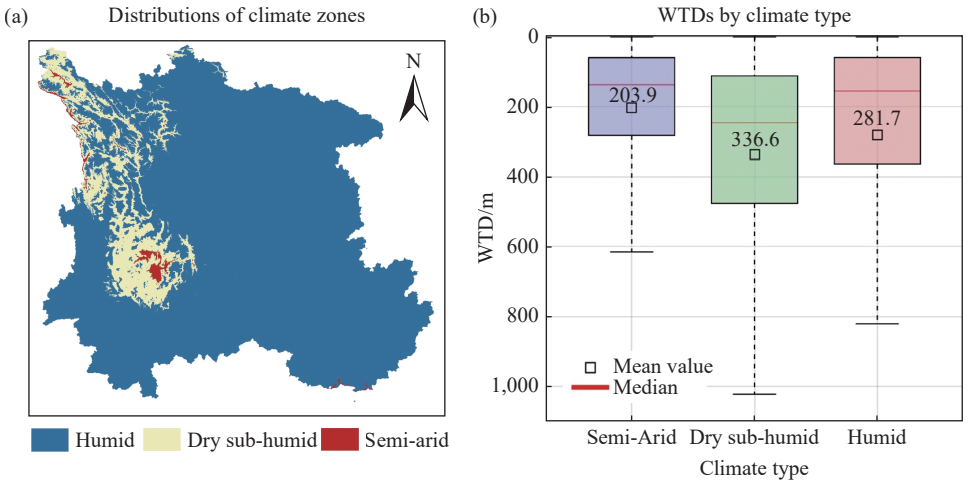


Fig. 6 Water Table Depths (WTDs) across different climate classes: (a) distributions of climate zones; (b) boxplots of WTDs across different climate types

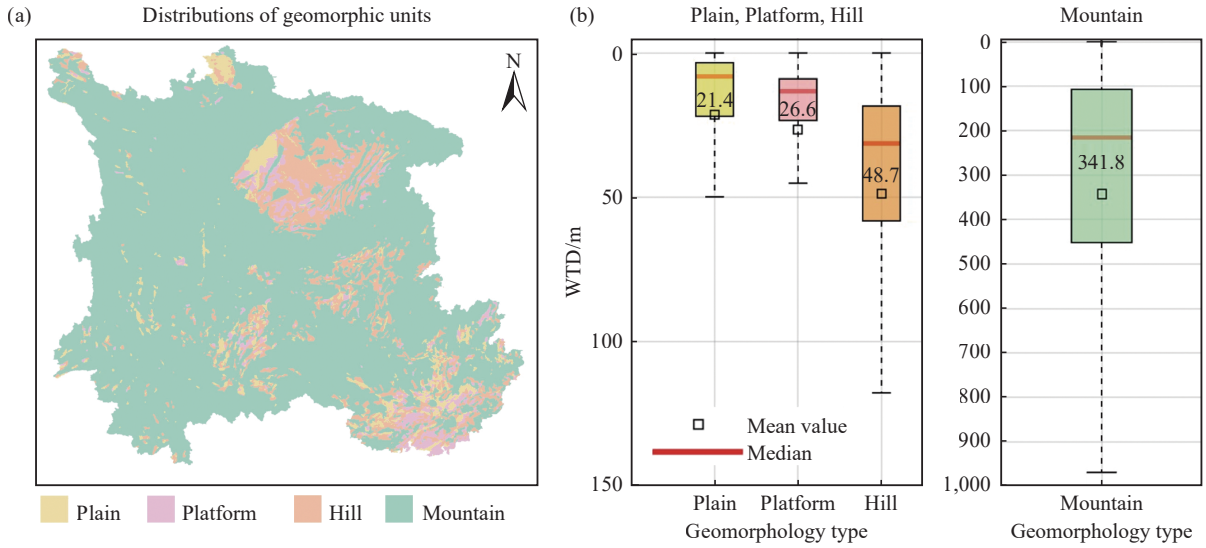


Fig. 7 Water Table Depths (WTDs) across different geomorphology types: (a) distributions of geomorphic units; (b) boxplots of WTDs across different geomorphic units

hydraulic gradients, and limited recharge zones (Flores et al., 2025; Huang et al., 2023). The wide interquartile range observed in the mountainous unit further underscores the heterogeneity of hydrogeological conditions, where localized shallow aquifers coexist with extensive deep groundwater systems.

3.2.3 Spatial distributions of water table depth over land cover types

Fig. 8 shows the spatial distribution of land cover types across SWC and their corresponding influences on WTD. The statistical analysis (Fig. 8b) demonstrates pronounced differences in WTD across land cover types. Urban areas exhibit the smallest mean WTD (40.9 m) while cropland shows a moderate mean depth (117.4 m). Forest and grassland display larger WTDs (295.0 m and 423.8 m, respectively), while unused land has the largest mean WTD (733.5 m). The broad interquartile ranges, especially for unused land, reflect the spatial variability in hydrogeological conditions and human impacts, highlighting the role of land cover in modulating groundwater systems through altered infiltration and extraction patterns (Jasechko et al., 2024; Li and Rodell, 2024; Niazi et al., 2024; Tanguy et al., 2023; Longhuan Wang et al., 2024).

3.2.4 Spatial distributions of water table depth over karst aquifer types

Fig. 9 presents a comparison of WTD across three aquifer types: Continuous carbonate rock, discontinuous carbonate rock, and non-karst areas. The mean WTD values are 222.4 m for continuous carbonate rock, 395.4 m for discontinuous carbonate rock, and 275.3 m for non-karst areas. The boxplot (Fig. 9b) reveals that discontinuous

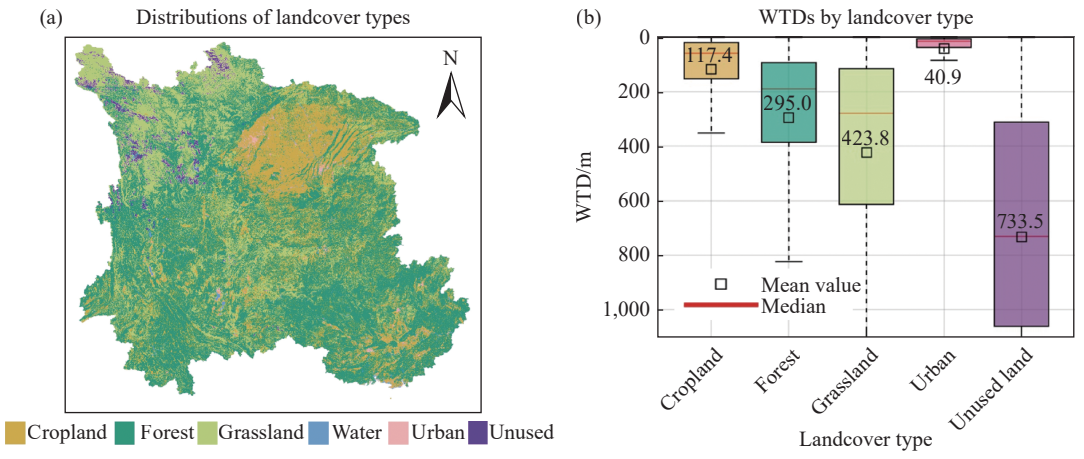


Fig. 8 Water Table Depths (WTDs) across different land cover types: (a) distributions of land cover types; (b) boxplots of WTDs over different land cover types

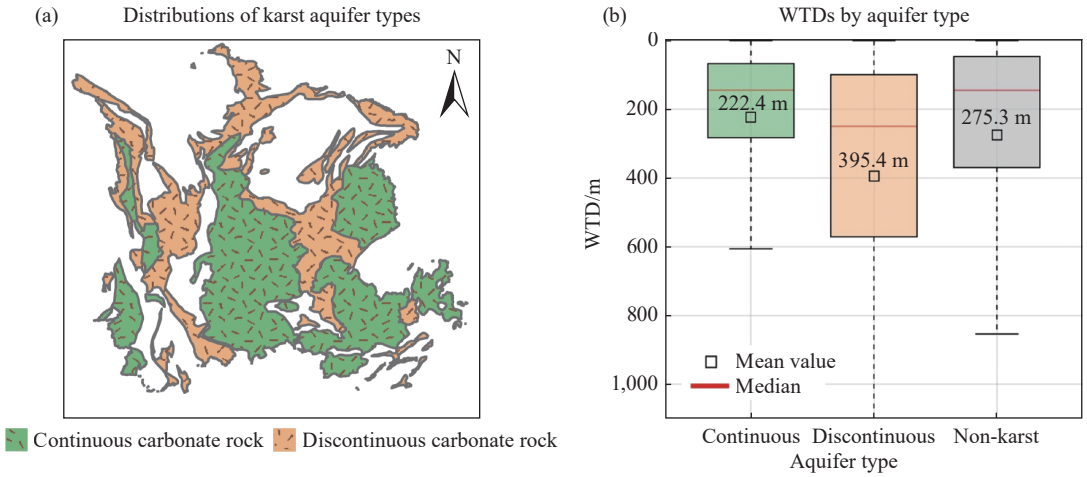


Fig. 9 Water Table Depths (WTDs) across different karst aquifer types: (a) distributions of karst aquifer types; (b) boxplots of WTDs over different karst aquifer types

carbonate rock aquifers exhibit the largest WTD with a wider interquartile range, indicating greater variability, while continuous carbonate rock aquifers show the smallest and least variable WTD. Non-karst areas fall between these two, with moderate depth and variability.

The differences in WTD among these aquifer types can be attributed to the hydrogeological characteristics inherent to karst systems (Ford and Williams, 2007). Continuous carbonate rock aquifers, with their well-connected fracture networks and efficient conduit flow, facilitate easier groundwater recharge and storage, leading to shallower water tables (Cooke et al., 2006). In contrast, discontinuous carbonate rock aquifers, characterized by fragmented rock units and poor hydraulic connectivity, result in delayed recharge and deeper water tables due to increased flow resistance and limited storage capacity (Medici et al., 2021). Non-karst areas, typically composed of porous or fractured non-soluble rocks, exhibit intermediate WTD influenced by local lithology and recharge patterns. The underlying cause for these variations likely stems from the degree of karstification and rock continuity, where continuous aquifers promote rapid water movement and shallow water tables, while discontinuous aquifers tend to exhibit deeper water tables through complex flow paths and reduced infiltration efficiency (Hao et al., 2025; LaFleur, 1999; Lu et al., 2024; Stevanović, 2015). It should be noted, however, that this inference does not incorporate the model simulation accuracy and uncertainty; thus, a more detailed analysis that considers the model characteristics would be beneficial (see Section 5.1).

Furthermore, the relationship between climate and WTD in karst is mediated by these hydrogeological properties. In well-developed karst area, continuous aquifers with efficient conduit networks (mean WTD: 222.4 m), recharge from high-intensity monsoon rainfall is rapidly transmitted through the system, often preventing the development of very deep water tables despite high potential evapotranspiration. Conversely, in discontinuous or poorly karstified carbonate rocks (mean WTD: 395.4 m), limited and delayed recharge, combined with the same climatic drivers, results in larger and more climatically sensitive water tables. Thus, the interaction between climate forcing (recharge) and hydrogeological architecture (storage and transmission) ultimately determines the observed WTD spatial patterns.

3.3 Analysis of anthropogenic stress on water table depth variability

Fig. 10 presents the spatial interactions between anthropogenic stress and WTD variability in Southwest China (SWC). Panel (a) illustrates provincial boundaries as a geographical reference, while panel (b) reproduces the WTD (previously shown in Fig. 1) to provide contextual comparison. Fig. 10c shows the anthropogenic stress intensity (0–99%) illustrating human modification patterns from minimal (green) to intensive (pink) landscape alteration. The subsequent analyses (Fig. 10d–10f) focus on the local spatial associations identified through local spatial correlation and bivariate LISA.

Fig. 10d reveals pronounced spatial heterogeneity in correlation patterns between WTD and anthropogenic stress, highlighting the contrasting responses of WTD to anthropogenic stress across

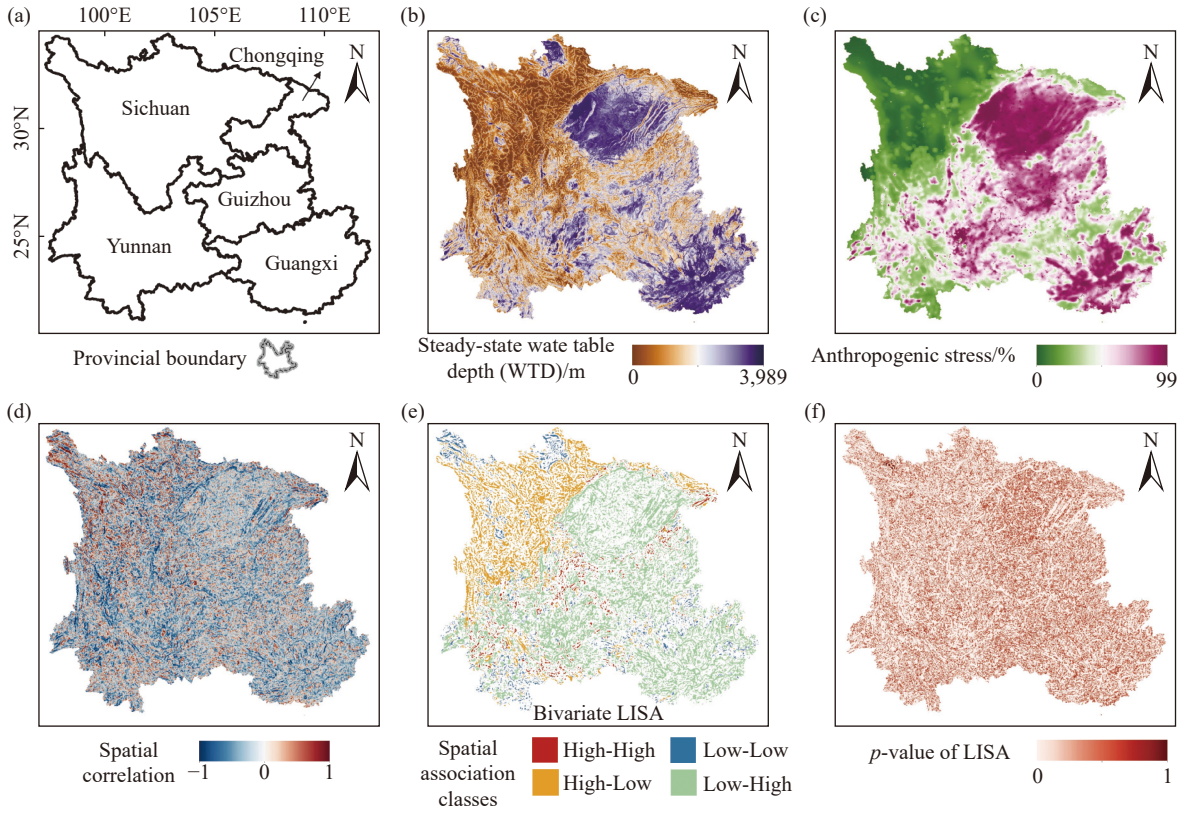


Fig. 10 Spatial associations between steady-state Water Table Depth (WTD) and anthropogenic stress in Southwest China

Notes: (a) provincial boundary map; (b) steady-state WTD distribution; (c) anthropogenic stress; (d) local spatial correlation between WTD and anthropogenic stress; (e) bivariate LISA cluster classification; (f) statistical significance (p-values) of the LISA results. Panels (b) and (c) are reproduced here for comparison purposes

provinces. Negative correlations dominate approximately 65% of the study area, particularly throughout eastern Sichuan Basin and Guangxi Province, indicating widespread inverse relationships between human modification intensity and WTD. In particular, in Guangxi Province, negative correlations dominate, reflecting the decoupling between deep aquifers and surface-level anthropogenic activity. Conversely, positive correlations cluster predominantly in the northwestern portion of Sichuan Province and central Yunnan Province, suggesting localized areas where human activities coincide with deeper water tables. This spatial pattern likely reflects the complex hydrogeological setting of karst terrains in SWC, where rural settlements and agricultural activities are concentrated in valleys with naturally larger WTD conditions, combined with potential groundwater extraction effects in these areas.

Fig. 10e displays the bivariate LISA classification, revealing four distinct categories of spatial relationships. High-High clusters (areas with significant positive spatial autocorrelation where both anthropogenic stress and water table depth exceed regional means) are predominantly concentrated in urbanized areas of central Sichuan Province and Yunnan Province, particularly throughout the Chengdu Plain and Chongqing metropolitan region. These zones represent locations of intensive human modification coupled with deeply incised water tables, likely resulting from concentrated groundwater extraction for municipal and industrial uses. Low-Low clusters (significant positive spatial autocorrelation with both variables below regional means) are primarily distributed across western Sichuan and northwestern Yunnan, corresponding to high-elevation regions with minimal human impact and naturally shallow groundwater tables characterized by high recharge potential. High-Low clusters (significant negative spatial autocorrelation featuring high anthropogenic stress with low water table depth) appear scattered throughout Guizhou Province, particularly in its central karst plateau region, reflecting areas where human settlement patterns overlap with complex hydrogeological systems featuring naturally deep water tables. Low-High clusters (significant negative spatial autocorrela-

tion showing low anthropogenic stress with high water table depth) are predominantly located in southeastern Yunnan and scattered portions of southern Sichuan, indicating regions where natural groundwater systems remain relatively undisturbed despite moderate human pressure. The statistical significance of these spatial patterns, as shown in Fig. 10f, confirms the robustness of these associations ($p < 0.05$ for all classified clusters).

Overall, these findings reveal a strong spatial heterogeneity in the interaction between anthropogenic stress and water depth in SWC. Eastern Sichuan, Chongqing, and central Yunnan exhibit spatially coherent clusters of high vulnerability, where intensive human activities overlap with shallow water tables. By contrast, southern Yunnan, Guizhou and Guangxi largely reflect natural hydrogeological control, with deeper water tables relatively insulated from direct anthropogenic influence. This spatially explicit understanding is critical for targeting management interventions, as regions with Low–High and High–High clusters represent priority zones for groundwater protection and monitoring.

4 Discussion

4.1 Limitations

While the GLOBGM model represents a significant advancement in global-scale groundwater modeling, several limitations must be acknowledged when applying it to the complex hydrogeological conditions of SWC. The model's relatively simple two-layer schematization, while computationally efficient, may inadequately represent the complex stratigraphic heterogeneity and multi-aquifer systems characteristic of this region. The parameterization scheme, which relies primarily on available PCR-GLOBWB data without local calibration, likely introduces uncertainties in hydraulic conductivity and storage parameter estimation, particularly in areas with limited observational constraints (de Graaf et al., 2017). The model can simulate large WTD values (up to several thousand meters) in deep sedimentary basins, but these simulations should be interpreted with caution due to the simplified aquifer representation and limited local calibration (de Graaf et al., 2017).

The validation of GLOBGM outputs remains notably limited, especially for the SWC region, which presents unique challenges for groundwater modeling. The model evaluation against USGS NWIS head observations, while demonstrating improvement over previous 5' models, primarily focused on the contiguous United States, leaving questions about its performance in geologically distinct regions like SWC (Verkaik et al., 2024). In this study, we validated GLOBGM against 17 monitoring wells with precise coordinates across SWC, which showed reasonable agreement. However, this small sample size is insufficient for a comprehensive regional validation. This validation gap is particularly concerning given the region's complex topography and hydrogeology.

The topographical complexity of SWC, characterized by dramatic elevation changes, intricate drainage patterns, and extensive river network dissection, presents fundamental challenges to the current model formulation (de Graaf and Stahl, 2022). The 30" resolution, while improved from previous global models, remains insufficient to capture the micro-topographical features and local-scale hydrological processes that dominate groundwater recharge and discharge patterns in this mountainous region. The treatment of surface water–groundwater interactions likely oversimplifies the complex exchange processes occurring in steep, fractured terrain, where local topography exerts dominant control on groundwater flow directions and velocities (de Graaf et al., 2015).

Furthermore, the model's limited ability to represent karst hydrogeology, which is widespread in SWC, constitutes a significant constraint. The current schematization does not explicitly account for preferential flow paths, sinkholes, and underground drainage networks that characterize karst systems, potentially leading to substantial misrepresentation of actual groundwater behavior (van Jaarsveld et al., 2025). The exclusion of detailed pumping data and artificial recharge activities further limits the model's capacity to accurately simulate anthropogenic impacts on groundwater systems in this rapidly developing region (de Graaf et al., 2024).

These limitations collectively suggest that while GLOBGM provides a valuable framework for regional-scale analysis, its application in topographically complex regions like SWC requires careful interpretation and should be complemented with local-scale investigations and validation efforts to ensure reliable representation of groundwater dynamics. Future improvements should focus on integrating higher-resolution hydrogeological characterization, well pumping data, and regional calibration parameters, coupled with the incorporation of higher-resolution topographic data to enhance simulation reliability in complex terrain regions. Particularly for SWC, future versions

would benefit from incorporating region-specific validation using local monitoring data and accounting for the unique hydrogeological characteristics of karst systems to better represent the complex groundwater dynamics in this critically important region.

4.2 Implications for groundwater protections

4.2.1 Implications for water resources management

The long-term trajectory of groundwater level rise across SWC, as indicated by a Sen's slope of –0.0285 m/y (corresponding to a decrease in WTD) from 1958 to 2015, suggests a net positive water balance over the multi-decadal scale, where natural recharge and other inputs have, on average, outpaced extraction. Although monsoonal precipitation maintains seasonal oscillations, the progressive decline in water tables, particularly after the early 2000s, underscores the cumulative stress imposed by both hydroclimatic variability and human withdrawals (Leijnse et al., 2024). The intensification of spring drawdowns, when evapotranspiration demand is high and recharge minimal, poses acute risks for aquifer sustainability and amplifies regional vulnerability to drought (Herbert and Döll, 2025). This dual control by climate and human activity necessitates integrated management strategies that balance seasonal variability with long-term groundwater dynamics.

Spatial analyses further reveal marked heterogeneity in groundwater vulnerability across climate zones, geomorphic settings, land cover types, and aquifer structures. Relatively shallow water tables in semi-arid regions (mean depth: 203.9 m) and in low-lying plains and platforms (21.4–26.6 m) are particularly exposed to contamination and overextraction pressures, especially where agricultural intensification and urban expansion coincide with limited recharge capacity (Chanapathi et al., 2019; Lu et al., 2025a). Urban areas (mean depth: 40.9 m) represent another zone of heightened risk, where aquifers with shallow water tables are subject to both quantity stress from withdrawals and quality degradation from pollutant inputs (Jasechko et al., 2024). By contrast, mountainous terrains and unused lands with deep water tables (>300 m) exhibit relative resilience, though their wide variability suggests localized vulnerabilities (Gnann et al., 2025). In terms of aquifer types, continuous carbonate rock systems sustain shallower water tables through efficient recharge, whereas discontinuous carbonate aquifers (mean depth: 395.4 m) are prone to deeper water tables and high variability, warranting closer observation of groundwater storage dynamics (Medici et al., 2021).

Taken together, these findings point to several spatial priorities for groundwater protection. The north-central alluvial plains, valley bottoms, and rapidly urbanizing basins should be considered focal areas for enhanced monitoring and regulation, as areas with shallow water tables in these zones face acute anthropogenic pressures. Semi-arid and dry sub-humid regions in western and transitional uplands also require careful attention, as even minor reductions in recharge or increases in pumping can propagate disproportionately into groundwater stress. Forested and grassland zones with larger WTD values provide buffering capacity, yet conservation policies are needed to ensure that land-use change does not erode their recharge functions.

From a management perspective, these patterns emphasize the importance of differentiated strategies aligned with spatial vulnerability. In high-risk zones, strict regulation of groundwater extraction, improved irrigation efficiency, and enhanced urban water recycling should be prioritized. Transitional and moderately vulnerable areas warrant strengthened early-warning systems and adaptive allocation mechanisms to mitigate seasonal drawdowns (Stewart et al., 2025). Low-risk but extensive regions with deep water tables require baseline monitoring to detect emerging pressures, especially under projected climate change (Wang et al., 2025). Expanding protection zones around areas with shallower water tables and intensive use, while integrating climate variability into allocation policies, will be essential for safeguarding both human water security and groundwater-dependent ecosystems in SWC.

4.2.2 Groundwater protection zone classification

The analysis of anthropogenic stress on WTD variability (Fig. 10) collectively demonstrates the complex interplay between human activities and groundwater systems across Southwest China, highlighting the necessity for regionally tailored water resource management strategies that account for both spatial heterogeneity in human pressure and the inherent diversity of hydrogeological settings. The pronounced provincial variations in human-groundwater interactions underscore the importance of considering jurisdictional boundaries in water governance frameworks, particularly given the transboundary nature of many

aquifer systems in this region.

By integrating spatial patterns of WTD with anthropogenic stressor data, we delineated four groundwater protection categories using empirically derived thresholds (Table 1, Fig. 11). Threshold values were adapted from established groundwater vulnerability frameworks (Allouche et al., 2017; National Research Council et al., 1993; Khadam and Kaluarachchi, 2003; Taghavi et al., 2022; Tian et al., 2024; Zhai et al., 2017) and modified to reflect the hydrogeological and socio-environmental conditions in SWC.

Four categories emerged, reflecting distinct levels of vulnerability and management priority. Special protection zones (0.67%) represent shallower water tables (<5 m) under high stress (>0.7), concentrated in alluvial plains and valley bottoms where agricultural and urban pressures are most acute. Priority monitoring zones (2.61%) are aeras with moderately shallow water tables (<10 m) with elevated stress (>0.5), forming transitional belts around the special protection zones. Long-term monitoring zones (3.53%) involve aeras with intermediate water tables (<20 m) still subject to significant human pressures, while extensive low-risk zones (80.42%) are located in highland regions characterized by deeper water tables (>20 m) and minimal anthropogenic impact. Approximately 12.76% of the study area could not be consistently classified due to data or hydrogeological complexity.

This classification highlights the concentration of high-risk groundwater systems in low-lying, densely modified landscapes, contrasting with more resilient conditions in sparsely populated highlands. By distinguishing areas of acute vulnerability from those requiring long-term surveillance, the zoning framework provides a practical basis for prioritizing monitoring and protection efforts, ultimately supporting the sustainable management of groundwater resources in SWC. More broadly, this zoning approach offers a spatially explicit translation of the identified groundwater–anthropogenic stress interactions, linking quantitative analysis of human impacts with actionable strategies for groundwater protection.

Table 1 Groundwater protection categories using empirically derived thresholds

Protection zone classification	Criterion	Representativeness	Area
Special protection zones	WTD < 5 m and anthropogenic stress > 0.7	Shallow groundwater under high human pressure	–9,108.10 km^2 (0.67%)
Priority monitoring zones	WTD < 10 m and anthropogenic stress > 0.5	Vulnerable groundwater with moderate human impact	–35,282.03 km^2 (2.61%)
Long-term monitoring zones	WTD < 20 m and anthropogenic stress > 0.5	Groundwater systems requiring ongoing observation	–47,753.28 km^2 (3.53%)
Low-risk zones	WTD > 20 m and anthropogenic stress < 0.5	Deep groundwater with minimal human impact	–1,087,435.06 km^2 (80.42%)
Other areas	-	-	–172,566.57 km^2 (12.76%)

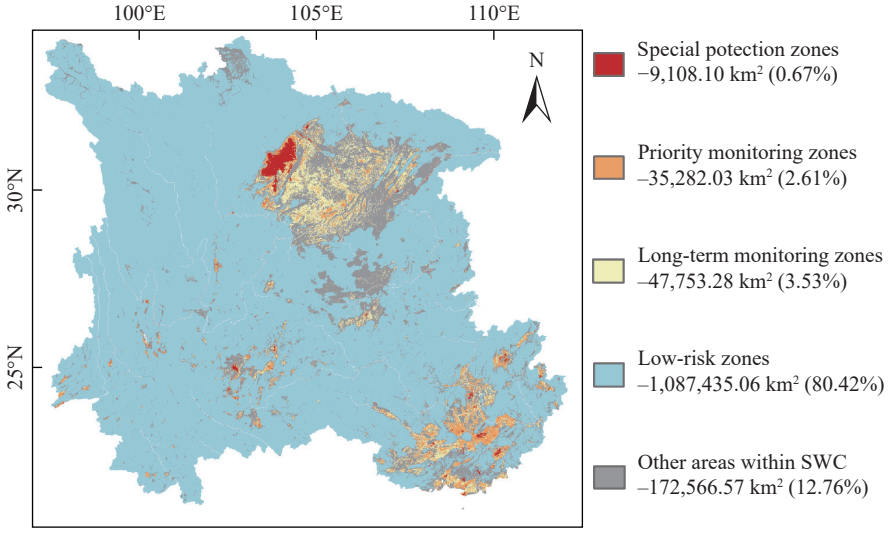


Fig. 11 Spatial distribution and statistics of groundwater protection zone for Southwest China

5 Conclusion

In this study, we provided a comprehensive assessment of Water Table Depth (WTD) dynamics across Southwest China (SWC) from 1958 to 2015, integrating temporal analysis, spatial characterization, and the influence of anthropogenic stress. Using outputs from the GLOBGM model, we examined long-term and seasonal variations in groundwater levels (as represented by WTD), the degree of coupling between shallow aquifers and precipitation–evapotranspiration balance, and the heterogeneity of groundwater systems across climate zones, geomorphic units, land cover categories, and karst aquifer types. The analysis was further extended to evaluate how anthropogenic pressures modulate spatial variability in WTD, employing spatial correlation and bivariate LISA to reveal the co-occurrence of human activity intensity and groundwater vulnerability. These findings were subsequently translated into a groundwater protection zoning framework, linking observed patterns of stress and hydrogeological sensitivity to differentiated management priorities.

The temporal analysis revealed an overall long-term tendency toward increasing groundwater levels (i.e., water table rise), as indicated by a Sen's slope of –0.0285 m/year for WTD, punctuated by episodic drawdowns during drought years. This overall decline in WTD (i.e., shallowing of the water table) trend suggests a net positive water balance over the multi-decadal scale. Seasonal oscillations driven by the Asian monsoon remain evident, with shallowest water tables following summer rainfall and deepest water tables during the late dry season. Shallow water tables (<1 m) display a strong positive correlation with precipitation–evapotranspiration, whereas deeper water tables (>5 m) are increasingly decoupled, reflecting buffering and delayed recharge processes.

Spatial analyses showed marked heterogeneity across environmental settings. WTD varied systematically with mean depths of 203.9 m in semi-arid zones, 336.6 m in dry sub-humid zones, and 281.7 m in humid zones. Geomorphology exerted a strong control, with mean WTDs of 21.4 m in plains, 48.7 m in hills, and 341.8 m in mountains. Land cover further modulated depths, with the shallowest mean WTDs found in urban areas (40.9 m) and the deepest in unused lands (733.5 m). Continuous karst aquifers exhibited shallower water tables (222.4 m) compared to discontinuous systems (395.4 m), highlighting the role of hydrogeological structure.

The interaction between anthropogenic stress and WTD variability revealed spatially coherent zones of vulnerability. Approximately 65% of the study area exhibited negative spatial correlations, while positive correlations clustered in specific provinces. Bivariate LISA classification identified statistically significant clusters ($p < 0.05$), pinpointing High–High clusters in urbanized basins, Low–Low clusters in high-elevation regions, and mixed High-Low/Low-High clusters in karst plateaus, thereby highlighting areas where groundwater systems are most vulnerable to anthropogenic modification.

A central, applied result of this synthesis is the development of a spatially explicit groundwater protection zoning framework (Fig. 11, Table 1). This framework integrates the key findings on WTD variability, anthropogenic stress, and their spatial associations to delineate four management categories: Special Protection, Priority Monitoring, Long-term Monitoring, and Low-risk zones. By classifying approximately 87% of the study area, it translates the complex spatial patterns identified through LISA and correlation analyses into actionable guidance for resource managers. The framework prioritizes interventions by identifying geographically explicit areas of acute vulnerability (e.g., areas with shallower water tables under high stress in alluvial plains) versus regions where deeper water tables provide a natural buffer. This moves beyond descriptive analysis to provide a direct, science-based tool for targeting monitoring investments, regulating groundwater extractions, and implementing protection measures, thereby enhancing the practical utility of our findings for sustainable groundwater governance in SWC.

This analysis underscores that while GLOBGM offers valuable insights at the regional scale, its simplified structure and limited representation of karst processes constrain its ability to capture local hydrogeological complexity. This is particularly evident in SWC, where rugged topography and fractured carbonate systems govern groundwater dynamics. The proposed protection zone classification helps address this scale limitation by providing a management-oriented lens to interpret model outputs.

Looking forward, advancing groundwater sustainability in SWC requires higher-resolution, higher-precision WTD datasets to better capture both vertical and lateral variability. Regional-scale modeling such as ParFlow-CLM (Condon and Maxwell, 2019; Lu et al., 2025c) can enhance the representation of surface–subsurface interactions in mountainous terrain. Equally important is the integration of more refined and disaggregated

anthropogenic activity data (Theobald et al., 2025), which would allow a clearer quantification of human–groundwater feedbacks. Moreover, to fundamentally unravel the mechanistic linkages between climate, karst hydrogeology, and water table dynamics identified in this study, we are implementing integrated surface-subsurface models with particle tracking (ParFlow-CLM and SLIM-FAST) (Maxwell et al., 2016; Siirila-Woodburn et al., 2023) at the catchment scale in SWC. Establishing robust data-sharing mechanisms across institutions will be critical to enable collaborative monitoring, calibration, and cross-validation, thereby supporting both local decision-making and the broader hydrological research community.

Data availability statement

All datasets employed in this study are publicly accessible. The water table depth dataset is derived from GLOBGM v1.0, available via the Yoda research data management service of Utrecht University (https://public.yoda.uu.nl/geo/UU01/44L775.html). Precipitation data are provided at https://doi.org/10.5281/zenodo.3114194, while evapotranspiration data are accessible through the National Tibetan Plateau/Third Pole Environment Data Center (https://doi.org/10.11888/RemoteSen.tpdc.272831). Geomorphology and land cover data were obtained from the Resource and Environmental Science Data Platform (https://www.resdc.cn/data.aspx?DATAID=124; https://www.resdc.cn/DOI/DOI.aspx?DOIID=54). The aridity index is available from Version 3 of the Global Aridity Index and Potential Evapotranspiration Database (https://doi.org/10.57760/sciencedb.nbsdc.00086). Karst aquifer extent data were sourced from the World Karst Aquifer Map (WHYMAP WOKAM, Version 1.0; https://www.whymap.org/whymap/EN/Maps_Data/Wokam/whymap_ed2017_map_g.html). Anthropogenic stress data are available at https://doi.org/10.6084/m9.figshare.7283087. Additional supporting datasets used for figures and charts are provided by the National Tibetan Plateau/Third Pole Environment Data Center (https://data.tpdc.ac.cn/).

Acknowledgements

This study was funded by the Project Supported by the Key Laboratory of Resource Environment and Sustainable Development of Oasis, Gansu Province (GORS202502), and Hainan Provincial 'Nanhaixinxing' Foundation of China (NHXXRCXM202352).

References

Adams KH, Reager JT, Rosen P, et al. 2022. Remote sensing of groundwater: current capabilities and future directions. Water Resource Research, 58: e2022WR032219. DOI：10.1029/2022WR032219.

Ahmad S, Shazil MS, Mahmood SA, et al. 2025. Quantifying climate change impacts on hydrological dynamics and sedimentation using GIS and SWAT + modelling. Hydrological Processes, 39: e70082. DOI：10.1002/hyp.70082.

Akhter T, Pokhrel Y, Felfelani F, et al. 2025. Implications of lateral groundwater flow across varying spatial resolutions in global land surface modeling. Water Resource Research, 61. DOI：10.1029/2024wr038523.

Akritas MG, Murphy SA, Lavalley MP. 1995. The theil-sen estimator with doubly censored data and applications to astronomy. Journal of the American Statistical Association, 90: 170−177. DOI：10.1080/01621459.1995.10476499.

Allouche N, Maanan M, Gontara M, et al. 2017. A global risk approach to assessing groundwater vulnerability. Environmental Modelling & Software, 88: 168−182. DOI：10.1016/j.envsoft.2016.11.023.

Anselin L. 1995. Local indicators of spatial association—LISA. Geographical Analysis, 27: 93−115. DOI：10.1111/j.1538-4632.1995.tb00338.x.

Anselin L, Sridharan S, Gholston S. 2007. Using exploratory spatial data analysis to leverage social indicator databases: the discovery of interesting patterns. Social Indicators Research, 82: 287−309. DOI：10.1007/s11205-006-9034-x.

Asoka A, Gleeson T, Wada Y, et al. 2017. Relative contribution of monsoon precipitation and pumping to changes in groundwater storage in India. Nature Geoscience, 10: 109−117. DOI：10.1038/ngeo2869.

Berghuijs WR, Luijendijk E, Moeck C, et al. 2022. Global recharge data set indicates strengthened groundwater connection to surface

fluxes. Geophysical Research Letters, 49: e2022GL099010. DOI：10.1029/2022GL099010.

Blaschke LL, Nian D, Bathiany S, et al. 2024. Spatial correlation increase in single-sensor satellite data reveals loss of Amazon rainforest resilience. Earth's Future, 12: e2023EF004040. DOI：10.1029/2023EF004040.

Brooks PD, Solomon DK, Kampf S, et al. 2025. Groundwater dominates snowmelt runoff and controls streamflow efficiency in the western United States. Communications Earth & Environment, 6: 341. DOI：10.1038/s43247-025-02303-3.

Chanapathi T, Thatikonda S, Pandey VP, et al. 2019. Fuzzy-based approach for evaluating groundwater sustainability of asian cities. Sustainable Cities and Society, 44: 321−331. DOI：10.1016/j.scs.2018.09.027.

Chávez García Silva R, Reinecke R, Copty NK, et al. 2024. Multi-decadal groundwater observations reveal surprisingly stable levels in southwestern europe. Communications Earth & Environment, 5: 387. DOI：10.1038/s43247-024-01554-w.

Chen C, Tian Y, Zhang, YK, et al. 2019. Effects of agricultural activities on the temporal variations of streamflow: Trends and long memory. Stochastic Environmental Research and Risk Assessment, 33: 1553−1564. DOI：10.1007/s00477-019-01714-x.

Chen Z, Auler AS, Bakalowicz M, et al. 2017. The world karst aquifer mapping project: Concept, mapping procedure and map of Europe. Hydrogeology Journal, 25: 771−785. DOI：10.1007/s10040-016-1519-3.

Condon LE, Atchley AL, Maxwell RM. 2020. Evapotranspiration depletes groundwater under warming over the contiguous United States. Nature Communications, 11: 873. DOI：10.1038/s41467-020-14688-0.

Condon LE, Maxwell RM. 2019. Simulating the sensitivity of evapotranspiration and streamflow to large-scale groundwater depletion. Science Advances, 5: eaav4574. DOI：10.1126/sciadv.aav4574.

Cooke ML, Simo JA, Underwood CA, et al. 2006. Mechanical stratigraphic controls on fracture patterns within carbonates and implications for groundwater flow. Sedimentary Geology, 184: 225−239. DOI：10.1016/j.sedgeo.2005.11.004.

Curran D, Gleeson T, Huggins X. 2023. Applying a science-forward approach to groundwater regulatory design. Hydrogeology Journal, 31: 853−871. DOI：10.1007/s10040-023-02625-6.

Cuthbert MO, Gleeson T, Moosdorf N, et al. 2019. Global patterns and dynamics of climate–groundwater interactions. Nature Climate Change, 9: 137−141. DOI：10.1038/s41558-018-0386-4.

de Graaf IEM, Marinelli B, Liu S. 2024. Global analysis of groundwater pumping from increased river capture. Environmental Research Letters, 19: 44064. DOI：10.1088/1748-9326/ad383d.

de Graaf IEM, Stahl K. 2022. A model comparison assessing the importance of lateral groundwater flows at the global scale. Environmental Research Letters, 17: 044020. DOI：10.1088/1748-9326/ac50d2.

de Graaf IEM, Sutanudjaja EH, Van Beek LPH, et al. 2015. A high-resolution global-scale groundwater model. Hydrology and Earth System Sciences, 19: 823−837. DOI：10.5194/hess-19-823-2015.

de Graaf IEM, Van Beek RLPH, Gleeson T, et al. 2017. A global-scale two-layer transient groundwater model: Development and application to groundwater depletion. Advances in Water Resources, 102: 53−67. DOI：10.1016/j.advwatres.2017.01.011.

Fan Y, Clark M, Lawrence DM, et al. 2019. Hillslope hydrology in global change research and Earth system modeling. Water Resources Research, 55: 1737−1772. DOI：10.1029/2018WR023903.

Fan Y, Li H, Miguez-Macho G. 2013. Global patterns of groundwater table depth. Science, 339: 940−943. DOI：10.1126/science.1229881.

Fang Z, Bogena H, Kollet S, et al. 2015. Spatio-temporal validation of long-term 3D hydrological simulations of a forested catchment using empirical orthogonal functions and wavelet coherence analysis. Journal of Hydrology, 529: 1754−1767. DOI：10.1016/j.jhydrol.2015.08.011.

Feng D, Gleason CJ. 2024. More flow upstream

and less flow downstream: The changing form and function of global rivers. Science, 386: 1305−1311. DOI：10.1126/science.adl5728.

Flores JA, Gleason CJ, Brown C, et al. 2025. Accelerating river discharge in high mountain asia. AGU Advances, 6: e2024AV001586. DOI：10.1029/2024AV001586.

Ford D, Williams PD. 2007. Karst hydrogeology and geomorphology. John Wiley & Sons.

Gleeson T, Cuthbert M, Ferguson G, et al. 2020. Global groundwater sustainability, resources, and systems in the Anthropocene. Annual Review of Earth and Planetary Sciences, 48: 431−463.

Gnann S, Baldwin JW, Cuthbert MO, et al. 2025. The influence of topography on the global terrestrial water cycle. Reviews of Geophysics, 63: e2023RG000810. DOI：10.1029/2023RG000810.

Gurdak JJ. 2017. Climate-induced pumping. Nature Geoscience, 10: 71−71. DOI：10.1038/ngeo2885.

Habib A. 2020. Exploring the physical interpretation of long-term memory in hydrology. Stochastic Environmental Research and Risk Assessment, 34: 2083−2091. DOI：10.1007/s00477-020-01883-0.

Hao H, Zhang J, Illman WA, et al. 2025. Insight into karst hydrological processes in the frequency domain: Critical frequency, phase difference, causality, and machine learning model. Journal of Hydrology, 663: 134150. DOI：10.1016/j.jhydrol.2025.134150.

Hartmann J, Moosdorf N. 2012. The new global lithological map database GLiM: A representation of rock properties at the Earth surface. Geochemistry, Geophysics, Geosystems, 13: 2012GC004370. DOI：10.1029/2012GC004370.

Herbert C, Döll P. 2025. Assessing groundwater drought hazard in groundwater depletion regions: recommendations for large-scale drought early warning systems. Water Resources Research, 61: DOI：10.1029/2024wr038684.

Hu T, Peng J, Qiu S, et al. 2024. Social-ecological heterogeneity drove contrasting tree cover restoration in south China karst. Communications Earth & Environment, 5: 484. DOI：10.1038/s43247-024-01641-y.

Hu Z, Chai L, Crow WT, et al. 2022. Applying a wavelet transform technique to optimize general fitting models for SM analysis: A case study in downscaling over the Qinghai–Tibet Plateau. Remote Sensing, 14: 3063. DOI：10.3390/rs14133063.

Huang P, Wang G, Guo L, et al. 2023. Most global gauging stations present biased estimations of total catchment discharge. Geophysical Research Letters, 50: e2023GL104253. DOI：10.1029/2023GL104253.

Huang Z, Yeh PJF, Pan Y, et al. 2019. Detection of large-scale groundwater storage variability over the karstic regions in southwest China. Journal of Hydrology, 569: 409−422. DOI：10.1016/j.jhydrol.2018.11.071.

Huggins X, Gleeson T, Famiglietti JS, et al. 2025. A review of open data for studying global groundwater in social–ecological systems. Environmental Research Letters, 20: 93002. DOI：10.1088/1748-9326/adf127.

Jalili S, Hamidi SA, Ghanbari RN. 2016. Climate variability and anthropogenic effects on lake urmia water level fluctuations, northwestern iran. Hydrological Sciences Journal, 61(10): 1759−1769. DOI：10.1080/02626667.2015.1036757.

Jasechko S, Seybold H, Perrone D, et al. 2024. Rapid groundwater decline and some cases of recovery in aquifers globally. Nature, 625: 715−721. DOI：10.1038/s41586-023-06879-8.

Jiang Y, Zhang C, Yuan D, et al. 2008. Impact of land use change on groundwater quality in a typical karst watershed of southwest China: A case study of the xiaojiang watershed, yunnan province. Hydrogeology Journal, 16: 727−735. DOI：10.1007/s10040-007-0259-9.

Kennedy CM, Oakleaf JR, Theobald DM, et al. 2019. Managing the middle: A shift in conservation priorities based on the global human modification gradient. Global Change Biology, 25: 811−826. DOI：10.1111/gcb.14549.

Khadam IM, Kaluarachchi JJ. 2003. Multi-criteria decision analysis with probabilistic risk assessment for the management of contaminated ground water. Environmental Impact Assessment Review, 23: 683−721. DOI：10.1016/S0195-9255(03)00117-3.

Kuang X, Liu J, Scanlon BR, et al. 2024. The changing nature of groundwater in the global water cycle. Science, 383: eadf0630. DOI: 10.1126/science.adf0630.

LaFleur RG. 1999. Geomorphic aspects of groundwater flow. Hydrogeology Journal, 7: 78–93. DOI: 10.1007/s100400050181.

Leijnse M, Bierkens FPM, Gommans HM, et al. 2024. Key drivers and pressures of global water scarcity hotspots. Environmental Research Letters, 19: 54035. DOI: 10.1088/1748-9326/ad3c54.

Li P, Tian R, Xue C, et al. 2017. Progress, opportunities, and key fields for groundwater quality research under the impacts of human activities in China with a special focus on western China. Environmental Science and Pollution Research, 24: 13224–13234. DOI: 10.1007/s11356-017-8753-7.

Li Y, Wang S, Peng T, et al. 2023. Hydrological characteristics and available water storage of typical karst soil in SW china under different soil–rock structures. Geoderma, 438: 116633. DOI: 10.1016/j.geoderma.2023.116633.

Liu K, Li X, Long X. 2021. Trends in groundwater changes driven by precipitation and anthropogenic activities on the southeast side of the hu line. Environmental Research Letters, 16: 94032. DOI: 10.1088/1748-9326/ac1ed8.

Liu Y, Lu C, Qiu B, et al. 2024. Spatiotemporally non-stationary evolution of groundwater levels in poyang lake basin driven by meteorological and hydrological factors. Science of the Total Environment, 950: 175244. DOI: 10.1016/j.scitotenv.2024.175244.

Long D, Xu Y, Cui YJ, et al. 2025. Unprecedented large-scale aquifer recovery through human intervention. Nature Communications, 16: 7296. DOI: 10.1038/s41467-025-62719-5.

Lu Z, Chai L, Liu S, et al. 2017. Estimating time series soil moisture by applying recurrent nonlinear autoregressive neural networks to passive microwave data over the Heihe River Basin, China. Remote Sensing, 9: 574. DOI: 10.3390/rs9060574.

Lu Z, He Y, Peng S, et al. 2023. Comprehensive evaluation of multisource soil moisture products in a managed agricultural region: An integrated hydrologic modeling approach. IEEE Journal of Selected Topics in Applied Earth Observations and Remote Sensing, 16: 1–17. DOI: 10.1109/JSTARS.2023.3289649.

Lu Z, Peng S, Wu T, et al. 2025a. Effects of irrigation and canal networks on groundwater–land surface interactions in the middle heihe river basin, china. Journal of Hydrology: Regional Studies, 60: 102532. DOI: 10.1016/j.ejrh.2025.102532.

Lu Z, Shen C, Zhan C, et al. 2025b. Quantifying multifactorial drivers of groundwater–climate interactions in an arid basin based on remote sensing data. Remote Sensing, 17: 2472. DOI: 10.3390/rs17142472.

Lu Z, Wei J, Yang X. 2024. Effects of hydraulic conductivity on simulating groundwater–land surface interactions over a typical endorheic river basin. Journal of Hydrology, 638: 131542. DOI: 10.1016/j.jhydrol.2024.131542.

Lu Z, Wu T, Lei J, et al. 2025c. Assessing a high-resolution integrated hydrologic model (ParFlow-CLM-HRB) in an endorheic basin of China. Journal of Hydrology, 661: 133579. DOI: 10.1016/j.jhydrol.2025.133579.

Lu Z, Yang X. 2024. Effects of microtopography on patterns and dynamics of groundwater–surface water interactions. Advances in Water Resources, 188: 104704. DOI: 10.1016/j.advwatres.2024.104704.

MacAllister DJ, Krishan G, Basharat M, et al. 2022. A century of groundwater accumulation in Pakistan and northwest India. Nature Geoscience, 15: 390–396. DOI: 10.1038/s41561-022-00926-1.

Maina FZ, Getirana A, Kumar SV, et al. 2024. Irrigation-driven groundwater depletion in the ganges-brahmaputra basin decreases the streamflow in the bay of bengal. Communications Earth & Environment, 5: 169. DOI: 10.1038/s43247-024-01348-0.

Mao H, Wang G, Liao F, et al. 2024. Spatiotemporal variation of groundwater nitrate concentration controlled by groundwater flow in a large basin: evidence from multi-isotopes (^{15}N, ^{11}B, ^{18}O, and ^{2}H). Water Resources Research, 60: e2023WR035299. DOI: 10.1029/2023WR035299.

Maxwell RM, Condon LE. 2016. Connections

between groundwater flow and transpiration partitioning. Science, 353: 377–380. DOI: 10.1126/science.aaf7891.

Maxwell RM, Condon LE, Kollet SJ, et al. 2016. The imprint of climate and geology on the residence times of groundwater. Geophysical Research Letters, 43: 701–708. DOI: 10.1002/2015GL066916.

Medici G, Smeraglia L, Torabi A, et al. 2021. Review of modeling approaches to groundwater flow in deformed carbonate aquifers. Groundwater, 59: 334–351. DOI: 10.1111/gwat.13069.

Mehboob MS, Kim Y. 2024. Impact of climate change on the hydrological projections over a western himalayan river basin and the associated uncertainties. Journal of Hydrology, 628: 130460. DOI: 10.1016/j.jhydrol.2023.130460.

Meles MB, Bradford S, Casillas-Trasvina A, et al. 2024. Uncovering the gaps in managed aquifer recharge for sustainable groundwater management: A focus on hillslopes and mountains. Journal of Hydrology, 639: 131615. DOI: 10.1016/j.jhydrol.2024.131615.

Moeck C, Grech-Cumbo N, Podgorski J, et al. 2020. A global-scale dataset of direct natural groundwater recharge rates: A review of variables, processes and relationships. Science of the Total Environment, 717: 137042. DOI: 10.1016/j.scitotenv.2020.137042.

National Research Council, Division on Earth and Life Studies, Commission on Geosciences, Environment and Resources, Committee for Assessing Ground Water Vulnerability. 1993. Ground water vulnerability assessment: Predicting relative contamination potential under conditions of uncertainty. National Academies Press. DOI: 10.17226/2050.

Niazi H, Wild TB, Turner SWD, et al. 2024. Global peak water limit of future groundwater withdrawals. Nature Sustainability, 7: 413–422. DOI: 10.1038/s41893-024-01306-w.

Ord JK, Getis A. 1995. Local spatial autocorrelation statistics: distributional issues and an application. Geographical Analysis, 27: 286–306. DOI: 10.1111/j.1538-4632.1995.tb00912.x.

Peng S, Ding Y, Liu W, et al. 2019. 1 km monthly temperature and precipitation dataset for China from 1901 to 2017. Earth System Science Data, 11: 1931–1946. DOI: 10.5194/essd-11-1931-2019.

Reinecke R, Gnann S, Stein L, et al. 2024. Uncertainty in model estimates of global groundwater depth. Environmental Research Letters, 19: 114066. DOI: 10.1088/1748-9326/ad8587.

Rodell M, Reager JT. 2023. Water cycle science enabled by the GRACE and GRACE-FO satellite missions. Nature Water, 1: 47–59. DOI: 10.1038/s44221-022-00005-0.

Scanlon BR, Fakhreddine S, Rateb A, et al. 2023. Global water resources and the role of groundwater in a resilient water future. Nature Reviews Earth & Environment, 4: 87–101. DOI: 10.1038/s43017-022-00378-6.

Sen PK. 1968. Estimates of the regression coefficient based on kendall's tau. Journal of the American Statistical Association, 63: 1379–1389.

Shen X, Niu L, Jia X, et al. 2025. Disentangling ecological restoration's impact on terrestrial water storage. Geophysical Research Letters, 52: e2024GL111669. DOI: 10.1029/2024GL111669.

Shi P, Tang H, Qu S, et al. 2024. Drought propagation in karst and non-karst regions in southwest China compared on a daily scale. Journal of Hydrology: Regional Studies, 51: 101628. DOI: 10.1016/j.ejrh.2023.101628.

Shu X, Xu L, Yang M, et al. 2023. Spatial distribution characteristics and migration of microplastics in surface water, groundwater and sediment in karst areas: the case of yulong river in guilin, southwest China. Science of the Total Environment, 868: 161578. DOI: 10.1016/j.scitotenv.2023.161578.

Siirila-Woodburn ER, Dennedy-Frank PJ, Rhoades A, et al. 2023. The role of atmospheric rivers on groundwater: Lessons learned from an extreme wet year. Water Resources Research, 59: e2022WR033061. DOI: 10.1029/2022WR033061.

Stevanović Z. 2015. Characterization of karst aquifer, in: Karst Aquifers—Characterization and Engineering. Springer, 47–125.

Stewart RD, Flury M, Ajami H, et al. 2025.

Emerging issues and research opportunities in vadose zone processes. Vadose Zone Journal, 24: e70030. DOI：10.1002/vzj2.70030.

Taghavi N, Niven RK, Paull DJ, et al. 2022. Groundwater vulnerability assessment: A review including new statistical and hybrid methods. Science of the Total Environment, 822: 153486. DOI：10.1016/j.scitotenv.2022.153486.

Tanguy M, Chevuturi A, Marchant BP, et al. 2023. How will climate change affect the spatial coherence of streamflow and groundwater droughts in Great Britain? Environmental Research Letters, 18: 064048. DOI：10.1088/1748-9326/acd655.

Taylor RG, Scanlon B, Döll P, et al. 2013. Ground water and climate change. Nature Climate Change, 3: 322–329. DOI：10.1038/nclimate1744.

Theobald DM, Oakleaf JR, Moncrieff G, et al. 2025. Global extent and change in human modification of terrestrial ecosystems from 1990 to 2022. Scientific Data, 12(1): 606. DOI：10.1038/s41597-025-04892-2.

Tian L, Hu L, Wang D, et al. 2024. Site-scale groundwater pollution risk assessment using surrogate models and statistical analysis. Journal of Contaminant Hydrology, 261: 104288. DOI：10.1016/j.jconhyd.2023.104288.

van Beek LPH, Wada Y, Bierkens MF. 2011. Global monthly water stress: 1. Water balance and water availability. Water Resources Research, 47(7): W07517. DOI：10.1029/2010WR009791.

van Jaarsveld B, Wanders N, Sutanudjaja EH, et al. 2025. A first attempt to model global hydrology at hyper-resolution. Earth System Dynamics, 16: 29–54. DOI：10.5194/esd-16-29-2025.

Verkaik J, Sutanudjaja EH, Oude Essink GHP, et al. 2024. GLOBGM v1.0: A parallel implementation of a 30 arcsec PCR-GLOBWB-MODFLOW global-scale groundwater model. Geoscientific Model Development, 17: 275–300. DOI：10.5194/gmd-17-275-2024.

Wada Y, Van Beek LPH, Van Kempen CM, et al. 2010. Global depletion of groundwater resources. Geophysical Research Letters, 37: 2010GL044571. DOI：10.1029/2010GL044571.

Wang L, Chen W, Haung G, et al. 2024. Characteristics of super drought in southwest China and the associated compounding effect of multiscalar anomalies. Science China Earth Sciences, 67: 2084–2102. DOI：10.1007/s11430-023-1341-4.

Wang LH, Jia B, Yuan X, et al. 2024. The slowdown of increasing groundwater storage in response to climate warming in the Tibetan Plateau. npj Climate and Atmospheric Science, 7: 286. DOI：10.1038/s41612-024-00840-w.

Wang Z, Chen W, Piao J, et al. 2025. Synergistic effects of high atmospheric and soil dryness on record-breaking decreases in vegetation productivity over southwest China in 2023. npj Climate and Atmospheric Science, 8: 6. DOI：10.1038/s41612-025-00895-3.

Wu H, Fang S, Yu L, et al. 2023. Limited co-benefits of protected areas in southwest China under current climate change and human modification. Journal of Environmental Management, 330: 117190. DOI：10.1016/j.jenvman.2022.117190.

Xing X, Wang P, Wang X, et al. 2024. Dams alter the control pattern of watershed land use to riverine nutrient distribution: Comparison of three major rivers under different hydropower development levels in southwestern China. Water Research, 260: 121951. DOI：10.1016/j.watres.2024.121951.

Xu S, Dverstorp B, Guerfi R, et al. 2023. Development of a model for radionuclide transport in streams for biosphere assessment purpose. Journal of Environmental Radioactivity, 264: 107188. DOI：10.1016/j.jenvrad.2023.107188.

Yang C, Zhang YK, Liang X. 2018. Analysis of temporal variation and scaling of hydrological variables based on a numerical model of the sagehen creek watershed. Stochastic Environmental Research and Risk Assessment, 32: 357–368. DOI：10.1007/s00477-017-1421-0.

Yin Z, Xu Y, Zhu X, et al. 2021. Variations of groundwater storage in different basins of China over recent decades. Journal of Hydrology, 598: 126282. DOI：10.1016/j.jhydrol.2021.126282.

Zhai Y, Zhao X, Teng Y, et al. 2017. Groundwater

nitrate pollution and human health risk assessment by using HHRA model in an agricultural area, NE china. Ecotoxicology and Environmental Safety, 137: 130–142. DOI：10.1016/j.ecoenv.2016.11.010.

Zhang W, Zhao J, Zhang Z, et al. 2023. The economy–employment–environmental health transfer and embedded inequities of China's capital metropolitan area: A mixed-methods study. The Lancet Planetary Health, 7: e912–e924. DOI：10.1016/S2542-5196(23)00218-8.

Zheng C, Jia L, Hu G. 2022. Global land surface evapotranspiration monitoring by ETMonitor model driven by multi-source satellite earth observations. Journal of Hydrology, 613: 128444. DOI：10.1016/j.jhydrol.2022.128444.

Zhong Y, Tian B, Kim H, et al. 2025. Over 60% precipitation transformed into terrestrial water storage in global river basins from 2002 to 2021. Communications Earth & Environment, 6: 53. DOI：10.1038/s43247-024-01967-7.

Zhou S, Yu B, Lintner BR, et al. 2023. Projected increase in global runoff dominated by land surface changes. Nature Climate Change, 13: 442–449. DOI：10.1038/s41558-023-01659-8.

Zomer RJ, Xu J, Trabucco A. 2022. Version 3 of the global aridity index and potential evapotranspiration database. Scientific Data, 9: 409. DOI：10.1038/s41597-022-01493-1.